PAPER

Check for updates

Investigating the impact of non-ideal conditions on the performance of an RbGeI₃ perovskite solar cell through a combination of SCAPS-1D, machine learning and deep learning approaches

Tanvir Mahtab Khan, [ID] *[a] Md. Atik Shams,[b] Most. Marzia Khatun,[a] Tahmid Ahamed,[b] Manjuara Akter,[b] Shajedul Hasan Arman,[b] Mirza Md. Shakil,[b] Hafiz Al Asad[c] and Sheikh Rashel Al Ahmed [ID] *[a]

In this work, the SCAPS-1D simulator is used to design and analyze an RbGeI₃-based perovskite solar cell (PSC) with the structure FTO/ZnO/RbGeI₃/Cu₂O/Ni. The proposed structure is evaluated under ideal and experimentally motivated non-ideal conditions. Initially, significant parameters such as thickness, bandgap, and doping concentration corresponding to different layers are optimized under ideal conditions, and a maximum efficiency of 30.41% is achieved. However, when non-ideal parameters such as the realistic values of defect density at bulk and interfaces, parasitic resistances, reflection loss, and radiative and Auger recombination losses are introduced, the efficiency of the cell decreases from 30.41% to 19.68%. Although the performance of the proposed device declines substantially, it reflects real-life conditions for the lead-free RbGeI₃-based PSC. Additionally, to identify the most accurate algorithm in PSC design technology, seven machine learning and four deep learning algorithms are compared in this study. Among them, XGBoost provides optimum accuracy with an excellent R^2 value of 0.9999 and a lower MSE of 0.0038. Furthermore, the influence of individual non-ideal parameters on the efficiency of the proposed structure is investigated, and it is found that shunt resistance dominates the efficiency among the five features. Therefore, this theoretical study will help to minimize trial-and-error efforts in designing pragmatically efficient RbGeI₃-based PSCs.

1. Introduction

The increasing consumption of fossil fuels has contributed to environmental deterioration, causing climate change and global warming and prompting the need for sustainable energy sources like solar power.[1–3] Solar cells are a feasible and carbon-free substitute for fossil fuels, as they can reduce societal and environmental damage.[4] As the usage of electronic devices and electricity escalates due to expanding populations, technological advancements, and development in emerging nations, energy consumption also increases.[5–7] Currently, fossil fuels contribute over 80% of the global energy demand.[6] As a result, the amount of CO_2 emission in the atmosphere increases substantially and pollutes the ecosystem.[8] Therefore,

to overcome these challenges, solar energy is a promising solution because it is reliable and environmentally friendly.

Among the various types of photovoltaic (PV) materials, organic–inorganic halides are highly appealing due to their large absorption coefficient, tunable bandgap, higher diffusion length, effective solution processing, lightweight nature, and low cost.[9–11] Despite this, most of their structural and mechanical characteristics pose major obstacles to the stability and reliability of the designed structure.[12] It is well known that the mechanical and thermal stress during the fabrication phase and aging of PV devices cause micro-cracks, which reduce the performance of the perovskite solar cells (PSCs).[13] Furthermore, lead (Pb)-based perovskite PV structures can adversely affect human growth and cognitive development, presenting significant barriers to its extensive commercialization.[14–16] To combat this challenge, scientists have investigated the application of alternative divalent metal cations such as Sn^{2+} and Ge^{2+}.[6] These alternatives exhibit a +2 oxidation state and an outer electron configuration identical to that of Pb^{2+}, which make them suitable replacements for Pb in PSCs.[17] But Sn^{2+} ions easily oxidize to Sn^{4+}, which reduces the stability of

[a] Department of Electrical, Electronic and Communication Engineering, Pabna University of Science and Technology, Pabna 6600, Bangladesh. E-mail: tanvirshaikat92@gmail.com, rashel@pust.ac.bd

[b] Department of Computer Science and Engineering, University of Asia Pacific, 74/A Green Rd, Dhaka 1205, Bangladesh

[c] Department of Computer Science and Engineering, Daffodil International University, Birulia, Savar, Dhaka-1216, Bangladesh

Sn-based PSCs under ambient conditions.[6,16] Additionally, the ionic radius of Ge^{2+}, Sn^{2+}, and Pb^{2+} is 0.73, 1.35, and 1.49 Å, respectively.[10,18] The small ionic radius of Ge^{2+} reduces the possibility of lattice distortion, which improves the charge transport mechanism significantly.[15] Moreover, Ge ions are chemically stable and provide better conductivity compared to the other two ions, which make them suitable for use in perovskite materials.[10,15]

Among various Ge-based halide perovskite materials, $RbGeI_3$ can be used as a potential absorber due to its suitable bandgap ranging from 1.3 to 1.4 eV.[9,15] The thermometric characteristics of $RbGeI_3$ were first investigated in 1989 *via* XRD and Raman spectroscopy.[19] For the very first time in 2019, the electrical, structural, and magnetic characteristics of a cubic $RbGeI_3$ halide perovskite were investigated using first-principles density functional theory (DFT) calculations.[20] In the same year, another first-principles DFT study reports the structural, electrical, and optical characteristics of an $RbGeI_3$ halide perovskite and evaluates parameters such as frequency-dependent dielectric constants, lattice constants, photo-absorption coefficients, effective masses of charge carriers, exciton binding energies, and electronic band structures using PBEsol and HSE06 functionals.[21] The DFT analysis of the various properties of the $RbGeI_3$ inorganic perovskite material, including elastic, optoelectronic, thermoelectric, thermodynamic, and mechanical properties, has been performed by many research groups to investigate its potential as a light-harvesting material in PSCs.[9,13–15] Although various research groups have already designed $RbGeI_3$-based halide PSCs, the PV performance parameters are still below the Shockley–Queisser limit.[22] Therefore, further research should be conducted to enhance the PV performance of $RbGeI_3$-based PSCs.

Recently, a theoretical efficiency of 10.11% with a fill factor of 63.68% was obtained for the $RbGeI_3$-based p–i–n structure of an $FTO/TiO_2/RbGeI_3/NiO/Ag$ solar cell using the SCAPS-1D simulator.[10] Another numerical study reported an excellent efficiency of 23.8% for an $RbGeI_3$-based PV device with $CuCrO_2$ as the hole transport layer (HTL).[23] A superior PCE of 24.03% with a V_{oc} of 0.88 V, a J_{sc} of 33.83 mA cm^{-2}, and an FF of 79.85% was achieved for the $FTO/TiO_2/RbGeI_3/PTAA/Au$ architecture among the twenty-five unique configurations of $RbGeI_3$-based PSCs with various electron transport layers (ETLs) and HTLs.[9] In 2024, an optimum theoretical efficiency of 30.35% with a V_{oc} of 1.067 V, a J_{sc} of 33.15 mA cm^{-2}, and an FF of 85.82% was achieved for an $RbGeI_3$-based PSC with TiO_2 as the ETL and Sb_2S_3 as a potential HTL.[6]

However, all these theoretical investigations are based on ideal conditions, and there are still no experimental findings on the $RbGeI_3$ material as a light-harvesting layer in PV technology. As we know, there is typically a large mismatch between the outcomes of numerical and experimental investigations. In this case, the incorporation of experimentally motivated non-ideal conditions such as reflection losses, parasitic resistances, radiative and Auger recombination losses, and defect densities at the bulk and interfaces will bridge the gap between the theoretical and experimental results.[24–27] Despite the final

outcomes indicating significantly lower performance, they are more consistent with the experimental findings. Therefore, herein, we have introduced the non-ideal conditions into the proposed $RbGeI_3$-based PSC to mimic the experimental performance.

Machine learning (ML) and deep learning (DL) algorithms have significant potential in the design and fabrication of PV devices by enhancing efficiency, reducing costs, and minimizing trial and error time.[28,29] In the field of materials science, ML/DL algorithms can rapidly screen and predict the properties of novel PV materials, significantly reducing the time and costs associated with experimental discovery. Moreover, ML/DL algorithms can predict the efficiency of the designed solar cells based on input parameters and device architecture. Besides, they can provide insights by revealing hidden patterns and correlations in large simulation datasets that traditional methods might overlook. This approach not only accelerates the design and optimization of novel solar cell structures but also supports the development of next-generation PV devices with improved performance and reduced development time.[28,30] Various research groups have successfully incorporated numerous ML techniques, including linear regression (LR), random forest (RF), support vector regression (SVR), and gradient boosting (GB), and deep learning techniques, including artificial neural network (ANN), K-nearest neighbor (KNN), and light gradient boosting machine (LGBM) algorithms, to analyze the influence of material properties on the performance metrics of PV devices.[28,31–38] Their reports validate the significance of employing ML and DL algorithms in solar cell technology.

In this study, real-world factors such as defect density, resistance, reflection, and recombination losses are incorporated into the simulation of the $RbGeI_3$-based PSC, in contrast to the majority of existing simulation studies that primarily consider idealized (non-real) conditions. Initially, key layer parameters—including bandgap, thickness, and doping concentration—are optimized under ideal conditions to achieve maximum theoretical efficiency. Subsequently, experimentally motivated non-ideal conditions are introduced by applying bulk and interfacial defect states, series and shunt resistances, reflection loss, and radiative and Auger recombination losses to mimic experimental performance. Finally, among the seven ML and four DL models tested, the XGBoost model demonstrates the highest prediction accuracy. SHAP analysis further reveals that shunt resistance is the most influential factor affecting device efficiency.

2. Methods

2.1. SCAPS-1D simulation and modelling

In this numerical study, we used the one-dimensional solar cell capacitance simulator (SCAPS-1D) to design and investigate the impact of ideal and experimentally motivated non-ideal conditions on the PV performance of the $RbGeI_3$-based PSC. This simulator was designed and developed by researchers at the Department of Electronics and Information Systems (ELIS),
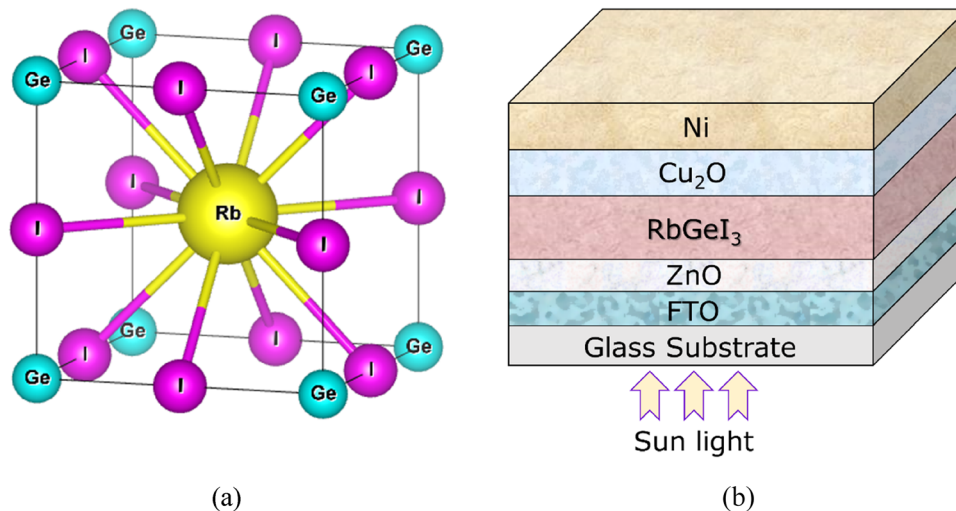
Fig. 1 (a) Cubic structure of RbGeI$_3$ and (b) schematic illustration of the designed PSC.

University of Ghent, Belgium.[39] This simulator was designed based on drift-diffusion equations, continuity equations, and Poisson's equations.[39,40] After entering the relevant materials' baseline parameters for each layer, the software can determine the PV performance metrics by solving the equations. Fig. 1(a) presents the cubic structure of the RbGeI$_3$ perovskite light-harvesting layer, which is extracted from the Materials Project open access database.[41] Fig. 1(b) illustrates the architecture of the RbGeI$_3$-based PSC, in which ZnO and Cu$_2$O are used as the ETL and the HTL, respectively. The device is simulated under AM 1.5G illumination at a power density of 1000 W m^{-2} and a temperature of 300 K.[10] The absorption coefficient (α) used for the individual layer can be calculated using the equation given below.

$$\alpha = A_\alpha \sqrt{(h\nu - E_g)}, \qquad (1)$$

where A_α is the pre-factor, $h\nu$ is the incident photon energy, and E_g is the bandgap of the individual layer of the designed PV device. In this numerical investigation, the physical parameters used for each layer are extracted from various published experimental and theoretical papers and listed in Table 1.[1,15,35,42–44] Additionally, the interface defect parameters used in this theoretical analysis are taken from various experimental reports in the literature and tabulated in Table 2.[42,45,46]

The energy band structure and energy level diagram of the proposed perovskite device are shown in Fig. 2(a) and (b). For efficient charge carrier transport, proper band alignment should be maintained between the active layer and charge transport layers.[35] The positions of energy levels at the interfaces can be directly assessed through the band offsets, namely the conduction band offset (CBO) and the valence band offset (VBO). Mathematically, the values of the CBO and VBO can be calculated using the following equations:[47]

$$CBO = X_{perovskite} - X_{ETL}, \qquad (2)$$

$$VBO = X_{HTL} + E_{g,HTL} - (X_{perovskite} + E_{g,perovskite}), \qquad (3)$$

where X and E_g represent the electron affinity and bandgap, respectively. According to the above equation, a positive CBO

Table 1 Physical parameters used for different layers in the proposed RbGeI$_3$-based PSC[1,15,35,42–44]

Parameter (unit)	n+-type window (FTO)	n-type ETL (ZnO)	p-type absorber (RbGeI$_3$)	p+-type HTL (Cu$_2$O)
Thickness (μm)	0.05	0.01–0.1^a	0.3–1.5^a	0.05–0.15^a
Band gap (eV)	3.6	3.3	1.40	2.17
Electron affinity (eV)	4.0	4.0	4.10	3.20
Dielectric permittivity (relative)	9.0	9.0	23.10	7.11
CB effective DOS (cm^{-3})	2.20×10^{18}	3.70×10^{18}	2.80×10^{19}	2.10×10^{17}
VB effective DOS (cm^{-3})	1.80×10^{19}	1.80×10^{19}	1.40×10^{19}	1.10×10^{19}
Electron thermal velocity (cm s^{-1})	10^7	10^7	10^7	10^7
Hole thermal velocity (cm s^{-1})	10^{07}	10^{07}	10^{07}	10^{07}
Electron mobility (cm^2 V^{-1} s^{-1})	100	100	28.60	200
Hole mobility (cm^2 V^{-1} s^{-1})	25.00	25.00	27.30	80
Donor density, N_D (cm^{-3})	10^{18}	10^{15}–10^{21} ^{a}	10^{09}	0
Acceptor density, N_A (cm^{-3})	0	0	10^{09}	10^{15}–10^{21} ^{a}
Defect type	SA	SA	SD	SD
Energy distribution		Gaussian	Gaussian	Gaussian
Defect density (cm^{-3})		10^{15}	10^{10}–10^{16} ^{a}	10^{15}

^{a} Variable.

Table 2 Parameters of interface layers[42,45,46]

Specifications (unit)	RbGeI$_3$/ZnO interface	Cu$_2$O/RbGeI$_3$ interface
Defect type	Neutral	Neutral
Capture cross-section of electrons (cm^2)	10^{-19}	10^{-19}
Capture cross-section of holes (cm^2)	10^{-19}	10^{-19}
Reference for defect energy level, E_t	Above the highest E_v	Above the highest E_v
Energy with respect to reference (eV)	0.6	0.6
Total density (cm^{-2})	10^{11}–10^{16}	10^{11}–10^{16}

with a value of 0.10 eV, which means a "spike-like" band offset, is formed at the RbGeI$_3$/ZnO interface. When the conduction band (CB) energy level of the ETL is greater than the CB energy level of the perovskite layer, a positive CBO, *i.e.*, a "spike-like" band structure, is formed.[48,49] This spike structure acts as a barrier for the flow of electrons.[49] On the other hand, a negative CBO, *i.e.*, a "cliff-like" band structure, is created when the CB energy level of the perovskite layer surpasses the CB energy level of the ETL layer.[48,49] Due to this cliff structure, the amount of electron accumulation at the perovskite/ETL interface

increases.[6] Consequently, the amount of recombination at the interface increases significantly.[6] According to the study, for better performance of the PV device, a positive CBO value of "spike-like" band formation is suitable compared to the "cliff-like" structure.[50]

To observe the effect of CBO on the recombination mechanism and device performance, the Nyquist plot is an excellent choice. The Nyquist plots for all devices are semicircular in nature.[51] The left side of the Nyquist plot indicates the impedance at high frequency, while the right side describes the impedance at low frequency.[52] Besides, the larger diameter of the Nyquist plot indicates better charge transport and reduced carrier recombination compared to the smaller diameter.[53] Here, a Nyquist plot is shown in Fig. 3(a) for various CBO values. The three CBO values were selected by varying the electron affinity of the ZnO ETL to investigate the sensitivity of the CBO to carrier recombination. From the figure, it is evident that positive CBO (spike) values have larger semicircle diameters in comparison to the negative CBO (cliff) value. Therefore, for spike-like band arrangements, the carrier recombination rate decreases significantly and eventually leads to
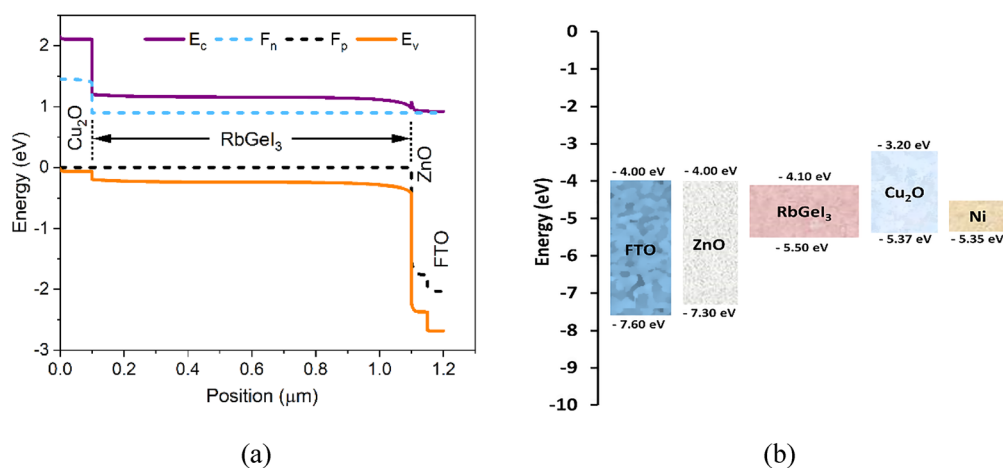

(a)

(b)

Fig. 2 (a) Energy band structure and (b) energy level diagram of the designed PSC.
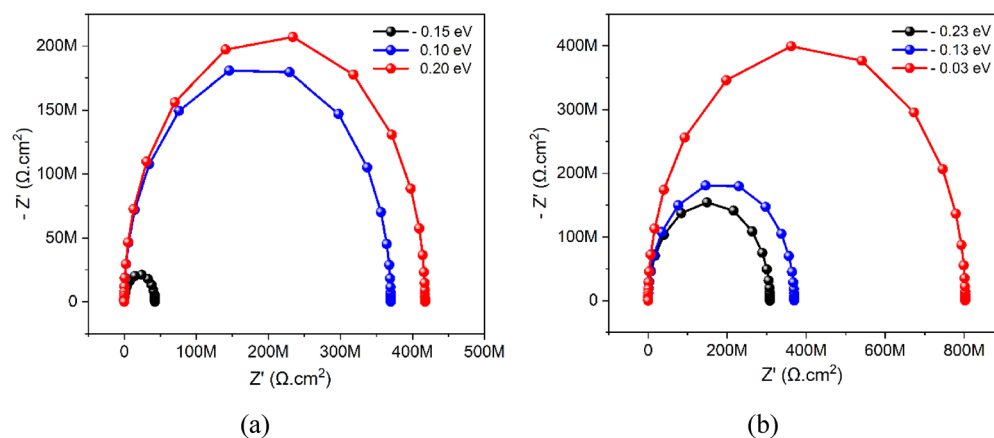

(a)

(b)

Fig. 3 Nyquist plots for (a) different CBO and (b) VBO values.

better device performance. In this numerical investigation, the CB energy level of the ZnO ETL surpasses that of the RbGeI$_3$ perovskite layer, with a positive CBO value of 0.1 eV, resulting in a restriction of electron injection at the RbGeI$_3$/ZnO interface, which will contribute to a reduced recombination rate. According to the theory, the PV performance parameters are maximized when the value of positive CBO ranges from 0 to 0.4 eV,[54] which closely aligns with our findings.

Additionally, for the efficient transport of holes from the perovskite layer to the back electrode, the value of VBO at the HTL/perovskite interface should be lower negative or positive.[6] A higher value of negative or positive VBO assists the collection of holes at the HTL/perovskite interface, which increases the recombination rate significantly.[47] As a result, the PV performance parameters of the solar cell decrease. Therefore, a lower value of VBO should be expected. Fig. 3(b) shows the impact of the VBO on charge recombination using the Nyquist plot. The different VBO values are selected by varying the electron affinity of the Cu$_2$O HTL to evaluate the sensitivity of device performance. From the figure, it can be seen that for lower negative values, the diameter of the Nyquist plot increased. As a result, the rate of recombination at the HTL/perovskite interface decreases, which aligns well with the theory.[47] In this study, using eqn (3), the value of VBO is calculated to be −0.13 eV. This parameter promotes easier transport of holes from the absorber to the back electrode through the HTL. Consequently, the rate of charge recombination at the back interface reduces substantially, resulting in improved overall device performance.

2.2. Machine and deep learning model development for solar cell performance optimization

In this study, various ML and DL models are employed to predict the efficiency of solar cells by analyzing their physical and electrical properties. The goal is to leverage data-driven techniques to accelerate the optimization process of solar cell performance while reducing the reliance on extensive experimental trials. Specifically, the study focuses on predicting the efficiency of solar cells based on five key experimentally motivated non-ideal input features: absorber defect density, series resistance, shunt resistance, reflection, and radiative recombination rate. These features are known to critically affect the internal loss mechanisms and energy conversion processes of solar devices. To comprehensively evaluate model performance and generalizability in predicting solar cell efficiency, a total of eleven models are explored, comprising seven traditional ML algorithms and four DL architectures. The ML models employed in this study include random forest (RF), support vector regressor (SVR), gradient boosting regressor (GBR), XGBoost, LightGBM, CatBoost, and multilayer perceptron (MLP). These algorithms are chosen for their proven effectiveness in handling non-linear relationships, robustness to noise, and suitability for small- to medium-sized datasets, making them ideal candidates for modeling the complex physical behavior of photovoltaic devices.[55] In addition to the ML models, four deep learning (DL) models are implemented:

artificial neural network (ANN), deep neural network (DNN), long short-term memory (LSTM), and convolutional neural network (CNN). These DL architectures are capable of learning intricate, high-dimensional feature representations and non-linear mappings, which are beneficial for capturing subtle dependencies among the input parameters.[56] Despite the relatively small dataset, regularization techniques, careful hyper-parameter tuning, and robust validation strategies are applied to prevent overfitting and enhance model generalization. All models are trained to predict solar cell efficiency based on five critical non-ideal input features and evaluated using regression metrics such as the R^2 score, mean squared error (MSE), and mean absolute error (MAE).

Before model training, a preliminary analysis is carried out to understand the statistical and physical relationships between the input parameters and solar cell efficiency. This involved both correlation-based and model-based feature significance evaluations. As illustrated in Fig. 4, the Pearson correlation heatmap is constructed to quantify the linear dependencies between each input feature and the target variable (Efficiency). The results show that shunt resistance has the highest positive correlation with Efficiency ($r = 0.44$), indicating its strong positive influence on performance. On the other hand, radiative recombination and absorber defect density exhibit moderate negative correlations ($r = -0.36$ and -0.21, respectively), reflecting their detrimental effects on solar cell output. Reflection and series resistance also show low negative correlations of -0.15 and -0.08, respectively.

To capture potential nonlinear interactions that correlation alone may not reveal, feature importance is further analyzed using the XGBoost algorithm, and the results are shown in Fig. 5. The feature importance ranking reaffirms the dominance of shunt resistance, followed by radiative recombination, absorber defect density, reflection, and series resistance. These findings not only validate the correlation outcomes but also highlight the capability of ensemble-based models to assess multivariate dependencies. Together, these analyses provided early-stage guidance for model design and confirmed the relevance of all five non-ideal input features. Given their physical interpretability and importance, no feature elimination or dimensionality reduction was performed prior to modeling.

The ranges of the non-ideal parameters were chosen based on the published data used mostly for solar cell simulation and fabrication. Table 3 shows the ranges, the total number of steps, and values of all these input material parameters. All possible combinations of the input parameters were utilized to generate 1024 unique samples and their corresponding power conversion efficiency. Here, a batch calculation in the SCAPS-1D is conducted to create a dataset for determining the effects of five non-ideal input parameters (absorber defect density, series resistance, shunt resistance, reflection, and radiative recombination rate) on device performance. These five experimentally motivated non-ideal input features characterize the electrical and optical loss mechanisms inherent to the solar cell structure and are critical in modeling its output performance.
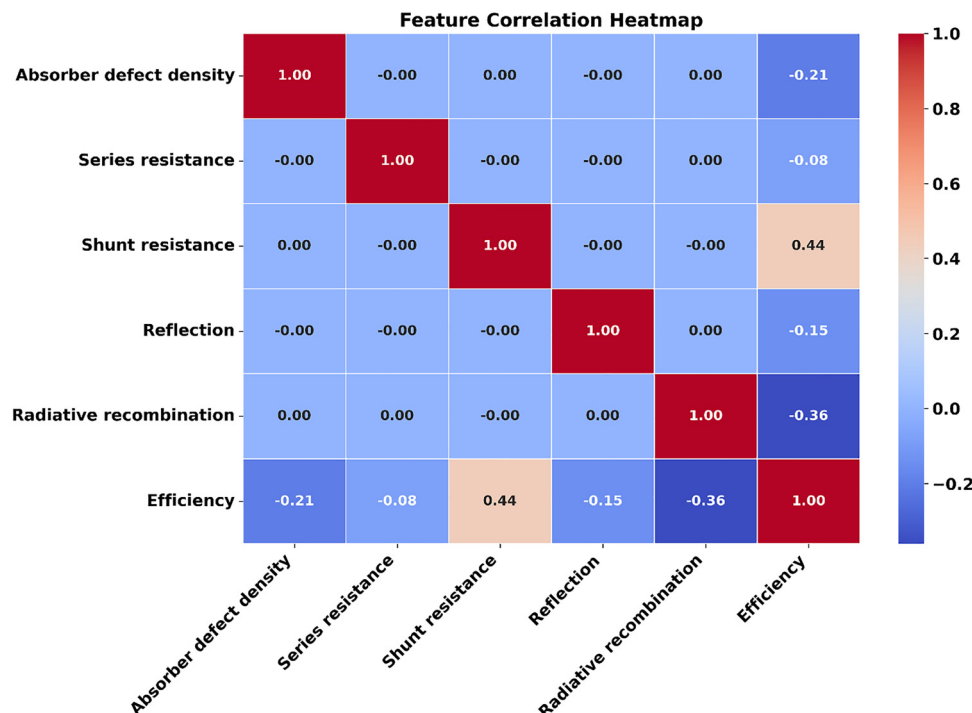
Feature Correlation Heatmap

Fig. 4 Pearson correlation heatmap to illustrate linear dependencies between each input feature and the target efficiency.

A preliminary inspection confirmed that the dataset contains no missing or null values, eliminating the need for data cleaning or imputation. To ensure reliable model validation and generalization, the dataset is partitioned into training and test subsets using an 80 : 20 split ratio. This separation helps prevent overfitting and ensures that all models are evaluated on unseen data.[57] Additionally, due to the variation in units and numerical scales among the input features, feature standardization is essential. StandardScaler from Scikit-learn is applied to normalize the data, ensuring that all features contribute equally during the training process. The scaler is first fitted on the training data and then applied to both the training and test sets to avoid information leakage.[58] This transformation scales each feature to have a mean of zero and a standard deviation of one. Such preprocessing is particularly crucial for models that

Table 3 Ranges and values of non-ideal parameters with steps

Parameters	Ranges	Steps	Values
Absorber defect density	10^{12}–10^{16}	4	10^{12}, 10^{13}, 10^{15}, 10^{16}
Series resistance	1.0–5.0	4	1.0, 3.0, 4.0, 5.0
Shunt resistance	10^1–10^5	4	10^1, 10^2, 10^4, 10^5
Reflection	0.05–0.25	4	0.05, 0.15, 0.2, 0.25
Radiative recombination rate	10^{-6}–10^{-11}	4	10^{-6}, 10^{-7}, 10^{-10}, 10^{-11}

rely on gradient-based optimization, including advanced neural architectures like CNN and LSTM, and machine learning models such as MLP. Proper scaling improves convergence speed and model stability, especially for techniques sensitive to feature magnitude. Moreover, to enhance model performance and ensure reliable predictions, a manual grid search strategy is implemented to systematically optimize the hyperparameters of all models.[59] For the seven ML models, important hyperparameters such as the number of estimators, tree depth, learning rate, kernel type, and regularization strength are tuned. Although MLP is a neural model in architecture, it is categorized as an ML model in this work due to its shallow structure and non-sequential design. For the four DL models, a grid search is performed to optimize parameters such as the number of layers, number of neurons per layer, activation functions (ReLU, sigmoid, and tanh), dropout rates, batch sizes, and learning rates. These hyperparameters play a pivotal role in controlling the model's capacity, convergence behavior, and regularization. During the tuning process, cross-validation is applied to prevent overfitting and to ensure generalizability across different data partitions. Each
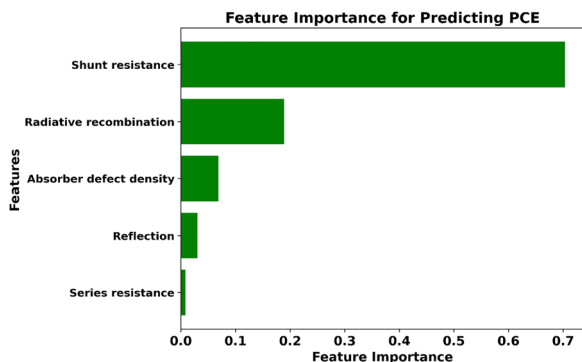
Feature Importance for Predicting PCE

Fig. 5 Feature importance for predicting PCE.

combination of hyperparameters is evaluated based on regression metrics including R^2, MAE, MSE, and RMSE.[59] These metrics collectively provide a balanced assessment of prediction accuracy, residual distribution, and error magnitude, enabling a robust comparison of model performance.

3. Results and discussion

3.1. Ideal conditions

Here, the theoretical performance limits of the RbGeI$_3$-based PSC are evaluated through simulations under ideal circumstances, assuming minimal defects, no optical loss, parasitic resistance free, and no recombination losses. Such conditions give an upper-bound estimate of the efficiency and important performance metrics of the solar cell. The PV outputs of V_{oc} = 1.10 V, J_{sc} = 31.73 mA cm^{-2}, FF = 87.04% and PCE = 30.41% are achieved by maintaining ideal conditions for the designed RbGeI$_3$-based PSC.

3.1.1. Effects of the thickness and bandgap of the RbGeI$_3$ perovskite layer on output parameters. The thickness and bandgap of the perovskite absorber layer in a solar cell are related since they both influence light absorption, charge carrier dynamics, and, ultimately, the efficiency of the solar cell. The thickness influences the amount of light absorbed and effective carrier collection, while the bandgap regulates the portion of the photon spectrum that is absorbed and transformed into electrical energy.

In this study, the absorber bandgap is adjusted from 1.25 eV to 1.6 eV, and the thickness is varied between 0.3 μm and 1.5 μm to examine the cell performance, as shown in Fig. 6. It is observed that increase in thickness has the greatest impact on J_{sc} and, in turn, efficiency. As the absorber thickness is increased within the range 0.3–1.5 μm, deeper light absorption creates a greater number of electron–hole pairs, increasing the J_{sc}.[33] The impact of thickness on FF and V_{oc} is less pronounced. However, additional thickness increases have little effect on performance metrics once a certain thickness of 1 μm is reached due to saturation of light absorption. A material requires a smaller thickness when its bandgap widens because it can absorb photons with more energy at shallower penetration depths. Wider bandgaps can result in higher V_{oc} and less absorption of lower-energy photons, diminishing J_{sc},[60] as evident from Fig. 6. While the FF has a smaller impact, efficiency follows the same pattern as J_{sc}. The conclusion is that the solar cell's ability to harvest light deteriorates with the widening of the band gap of RbGeI$_3$. A bandgap of 1.4 eV for the absorber is crucial in balancing V_{oc} and J_{sc} to maintain the highest possible PCE.

3.1.2. Effects of the thickness of the ETL and the HTL of the proposed structure on PV outputs. Solar cells require charge transport layers (ETL and HTL) since they are vital in improving efficiency, stability, and overall device performance. The absorber utilizes photoabsorption to generate electron–hole pairs. The ETL and HTL capture and transmit electrons and holes, respectively, while obstructing their counterparts. The ETL and HTL build energy barriers that allow the passage of only a particular charge carrier, minimizing recombination. The thickness of the ETL and the HTL is a key design parameter
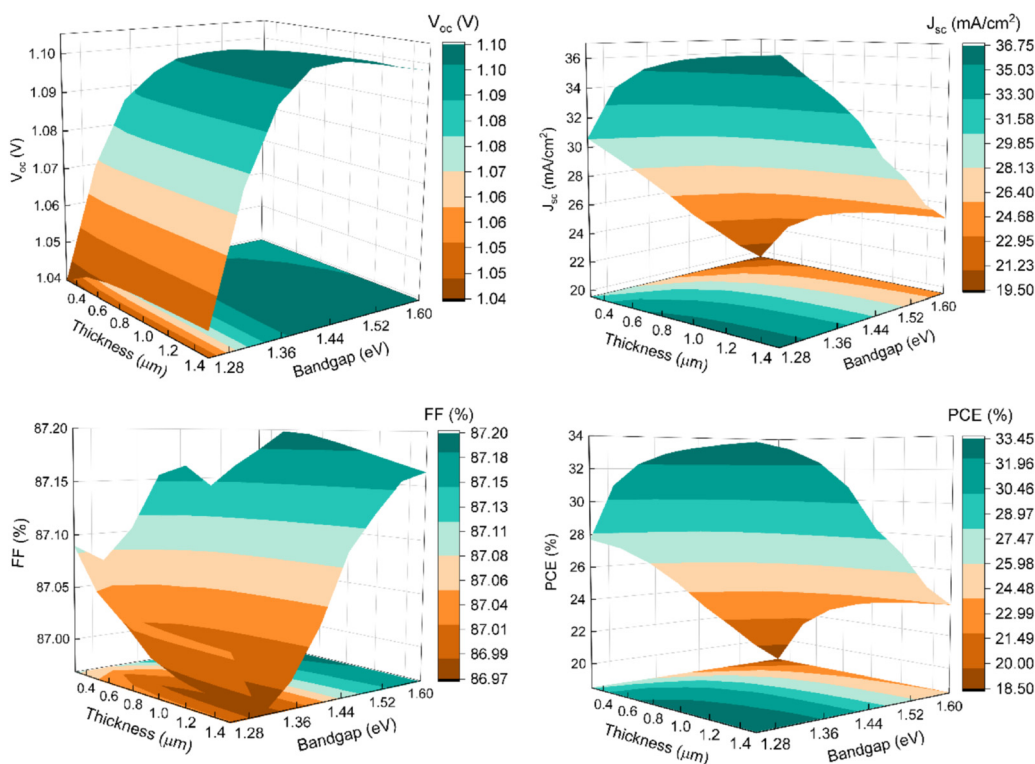

Fig. 6 Effects of the thickness and bandgap of the perovskite layer on the output metrics of the proposed PSC.
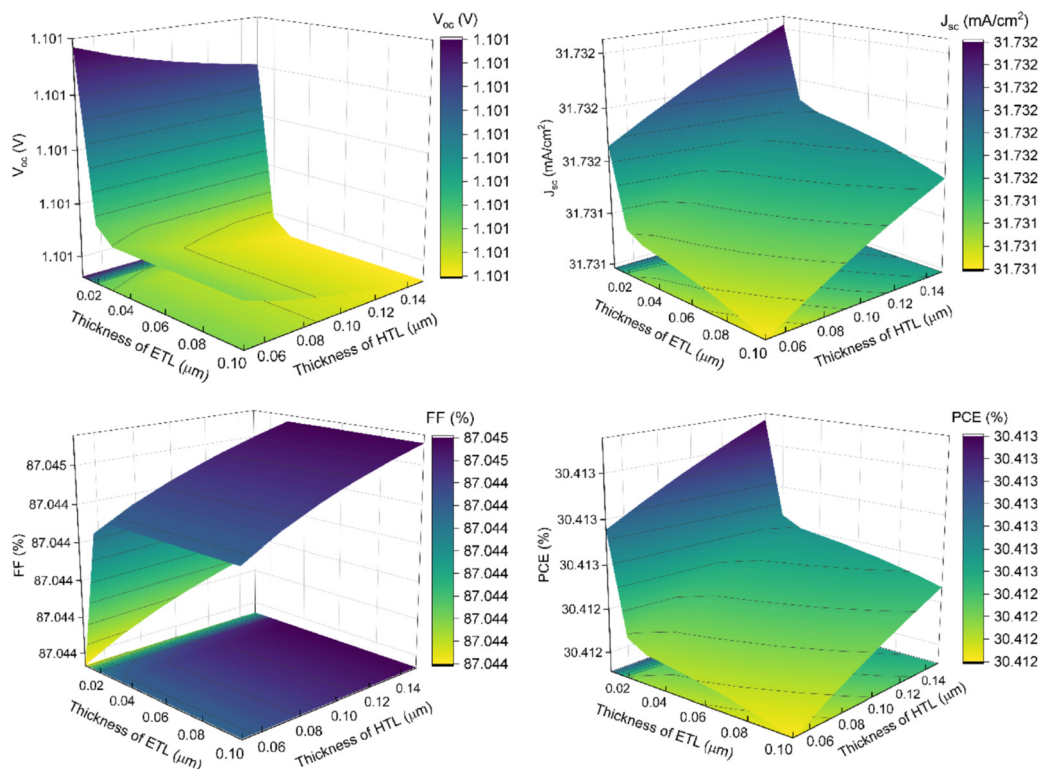
Fig. 7 Effects of the thickness of the ETL and the HTL on the output metrics of the proposed PSC.

that must be tuned to equalize charge extraction, limit recombination, and minimize resistance.[61] Fig. 7 illustrates the impact of ETL and HTL thicknesses on cell performance when varied within the ranges of 10–100 nm and 50–150 nm, respectively. The findings from Fig. 7 indicate that the cell performance declines slightly with enhanced ETL thickness. Reduced transparency is the consequence of both enhanced recombination and parasitic absorption as the ETL thickness increases.[62] In contrast, all the PV parameters, except V_{oc}, improved a little when the HTL thickness was varied between 50 and 150 nm. The device architecture may employ a thicker HTL layer that offers increased mobility and conductivity to create high performance and reproducible devices.[63] As the HTL is not required to be transparent, its thickness is less significant than that of the ETL. An ETL with a thickness of 50 nm and an HTL with a thickness of 100 nm are employed in this simulation to account for these factors.

3.1.3. Effects of the doping concentrations of the ETL and HTL of the proposed structure on PV outputs. A solar cell's performance is greatly influenced by the doping density in the ETL and the HTL, especially with regard to charge transfer, recombination, and overall efficiency. The doping density regulates the electric fields that separate the charge carriers at the absorber/HTL and ETL/absorber interfaces.[64] Fig. 8 shows the output characteristics of the constructed solar cell when the doping density is varied from 10^{15} cm^{-3} to 10^{21} cm^{-3} in both the ETL and the HTL, respectively. The doping density in the ETL exhibits limited influence on the overall device outcomes. This is attributed to the use of a thinner ETL

(50 nm) that has no discernible impact on device performance as long as the doping concentration in the ZnO ETL is far greater than that of RbGeI$_3$.[65] Conversely, Fig. 8 demonstrates that, except for J_{sc}, the cell's PV characteristics greatly improved as the HTL doping density increased. Greater bulk recombination results from increased dark current when the HTL is lowly doped.[65] This phenomenon results in a lower V_{oc}, whereas increasing the doping density increases the V_{oc} values, as shown in Fig. 8. Additionally, a weaker FF due to reduced HTL doping indicates a higher series resistance.[66] Consequently, V_{oc} and FF are the most affected metrics, simultaneously decreasing the device's efficiency. In the subsequent assessment procedures, the doping density is kept at 10^{18} cm^{-3} for both the ETL and the HTL.

3.2. Experimentally motivated non-ideal conditions

Solar cell simulations are often considered idealized and oversimplified because they rely on assumptions that do not fully capture real-world complexities. The idealized simulation provides valuable insights into the theoretical efficiency limits of solar cells. By comparing these results with practical constraints, researchers can identify key areas for material and device optimization, ultimately improving the real-world efficiency of photovoltaic systems. However, real-world applications require the consideration of material imperfections, resistive losses, recombination, and environmental influences. This study examines the impact of defect density, parasitic resistance, reflection, and radiative and Auger recombination losses in experimentally motivated non-ideal scenarios.
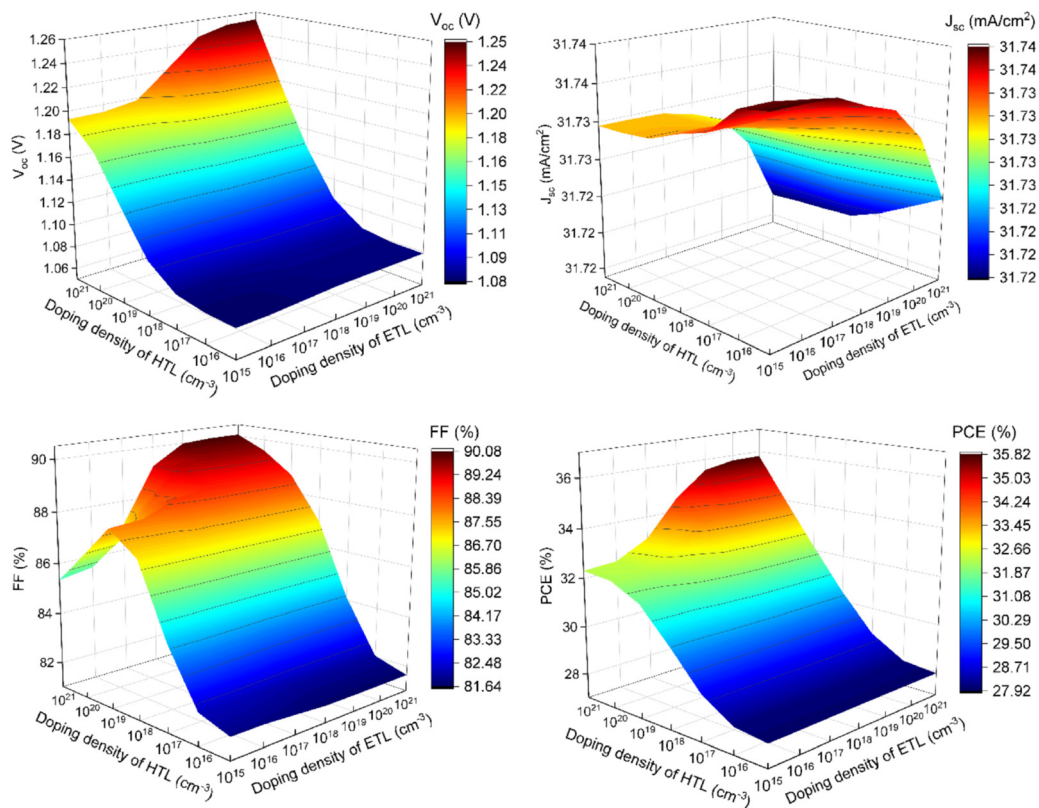
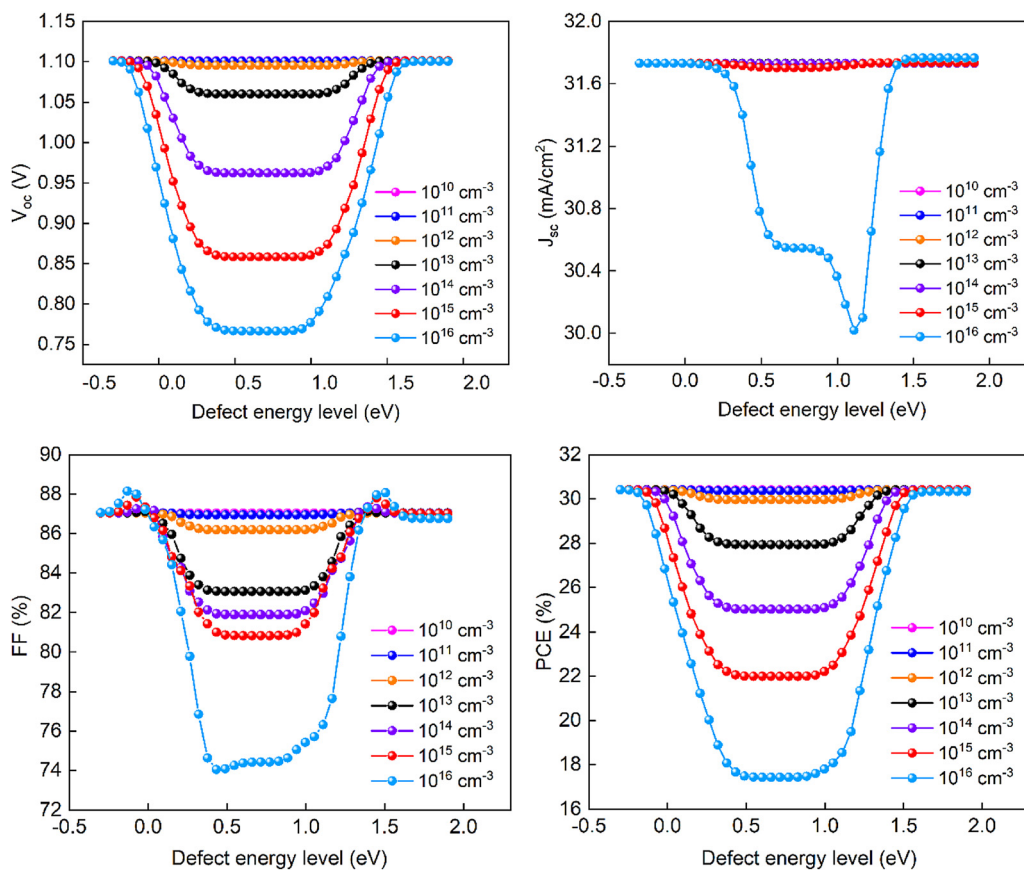Fig. 8 Effects of the doping density of the ETL and the HTL on the output metrics of the proposed PSC.

Fig. 9 Effects of different defect levels at different densities of the RbGeI$_3$ perovskite layer on PV outputs.

3.2.1. Effects of the defect density of the RbGeI$_3$ perovskite layer on PV outputs. The optoelectronic characteristics of thin-film devices are significantly influenced by defect states in bulk materials, which act as recombination sites for photo-generated carriers. Device performance at various defect energies and concentrations can offer a comparative analysis that can be used to optimize non-ideal settings, considering that defect level densities are heavily reliant on experimental process pathways. Fig. 9 depicts the solar output variables based on defect levels and their concentrations in the RbGeI$_3$ absorber. While the location of the defect level within the bandgap dictates its impact on recombination and carrier dynamics, recombination losses increase with defect concentration. There are two types of defects based on position: shallow and deep.[67] Shallow defects are located close to the conduction or valence bands, whereas deep defects are formed close to the mid-band gap energy. Additionally, shallow defects have a smaller impact on PSC performance than deep defects.[68] The data from Fig. 9 show that performance metrics decrease with larger defect concentrations at defect levels ranging from 0.3 to 1.4 eV, categorized as deep defects. For the perovskite layer, experimentally the value of the defect state is observed to range between 10^{10} cm^{-3} and 10^{17} cm^{-3}.[42–44] In this study, we have used a bulk defect density of 10^{14} cm^{-3}, which can be achieved experimentally. Therefore, at the optimized defect value of 10^{14} cm^{-3} with a level of 0.77 eV, the PV results are acquired

as follows: V_{oc} = 0.96 V, J_{sc} = 31.73 mA cm^{-2}, FF = 81.89%, and PCE = 25%. The severity of photovoltaic defects depends on their location, concentration, and energy level, leading to subjective conclusions.

3.2.2. Influence of interface defect density on cell performance. Bulk defects primarily lower carrier lifetime and diffusion length, but interface defects promote recombination and increase resistive loss. Additionally, mid-gap states may be produced by interface imperfections, impairing both the emission and absorption processes and negatively influencing the efficiency of photoconversion.[69] For further investigation, defect states are introduced at the ETL/absorber and HTL/absorber interfaces, with densities ranging from 10^{11} cm^{-2} to 10^{16} cm^{-2}. Fig. 10 shows that the device performance is more negatively impacted by greater defect concentrations at the HTL/absorber interface than by defects at the ETL/absorber interface. Higher defect states at the interfaces have the least impact on J_{sc} because bulk recombination predominates over interface recombination. Efficiency decreases as V_{oc} and FF drop together with larger defect densities. This considerable efficiency loss suggests rapid recombination at the interfaces, possibly caused by the development of intermediary trap states for carriers between the adjacent layers. Experimentally, the interface defect density is observed to be in the range of 10^{12}–10^{17} cm^{-2}.[44] Therefore, in our study, we have used an interface defect density of 10^{14} cm^{-2} for both the ETL/absorber and
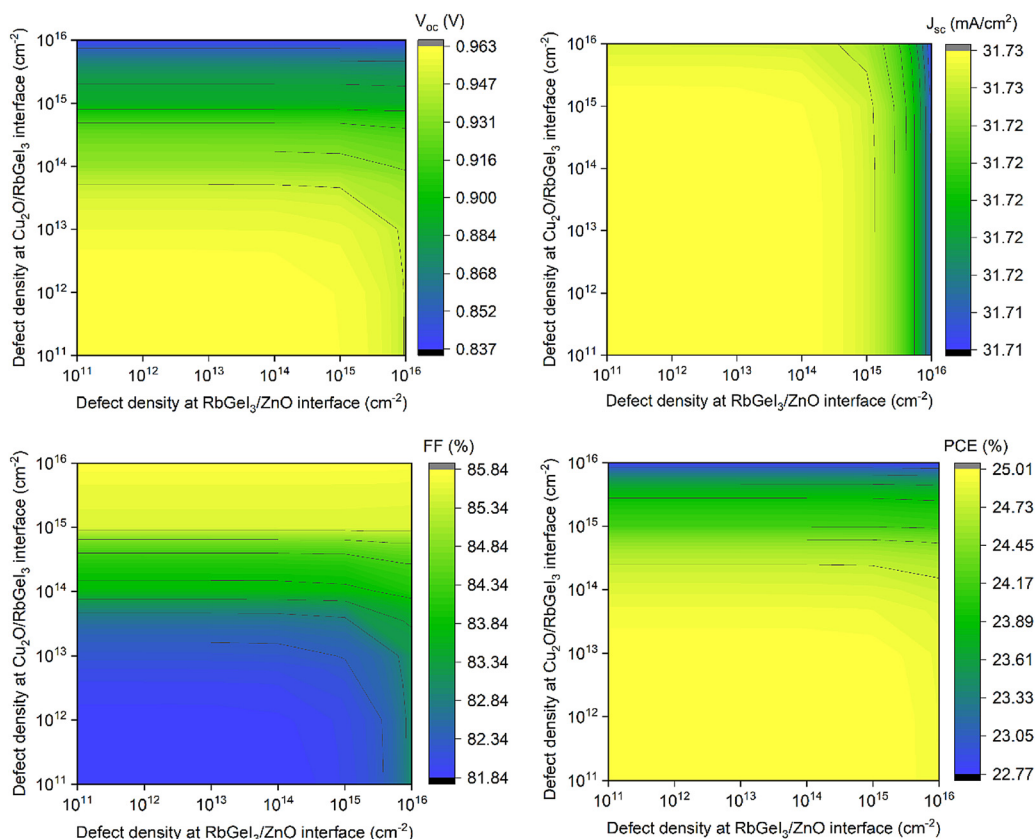

Fig. 10 Impact of defect density at ZnO/RbGeI$_3$ and RbGeI$_3$/Cu$_2$O interfaces on the performance metrics of the proposed PSC.
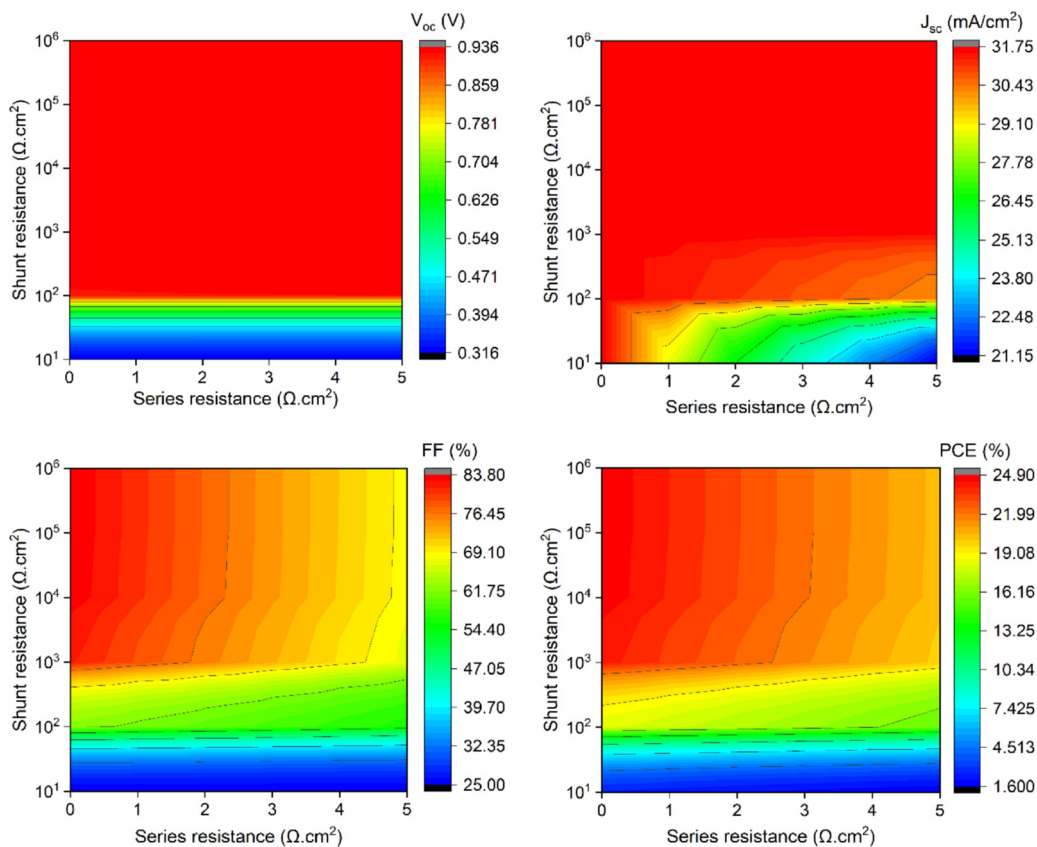
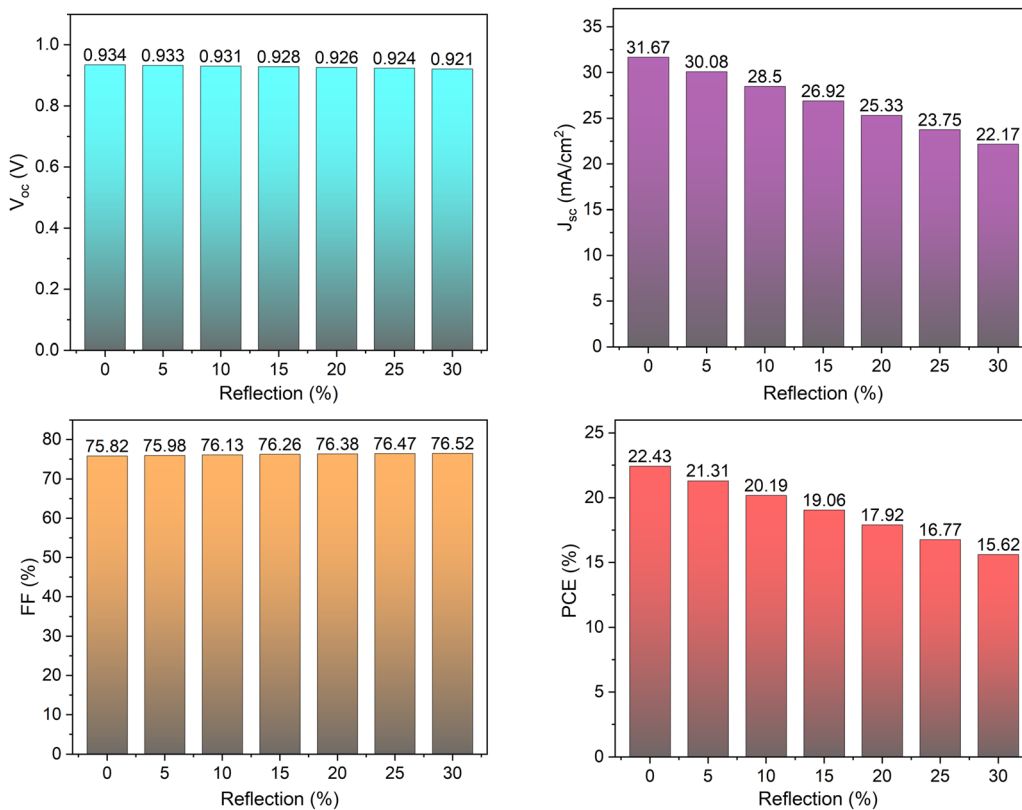**Fig. 11** Effects of series and shunt resistances on PV outputs.

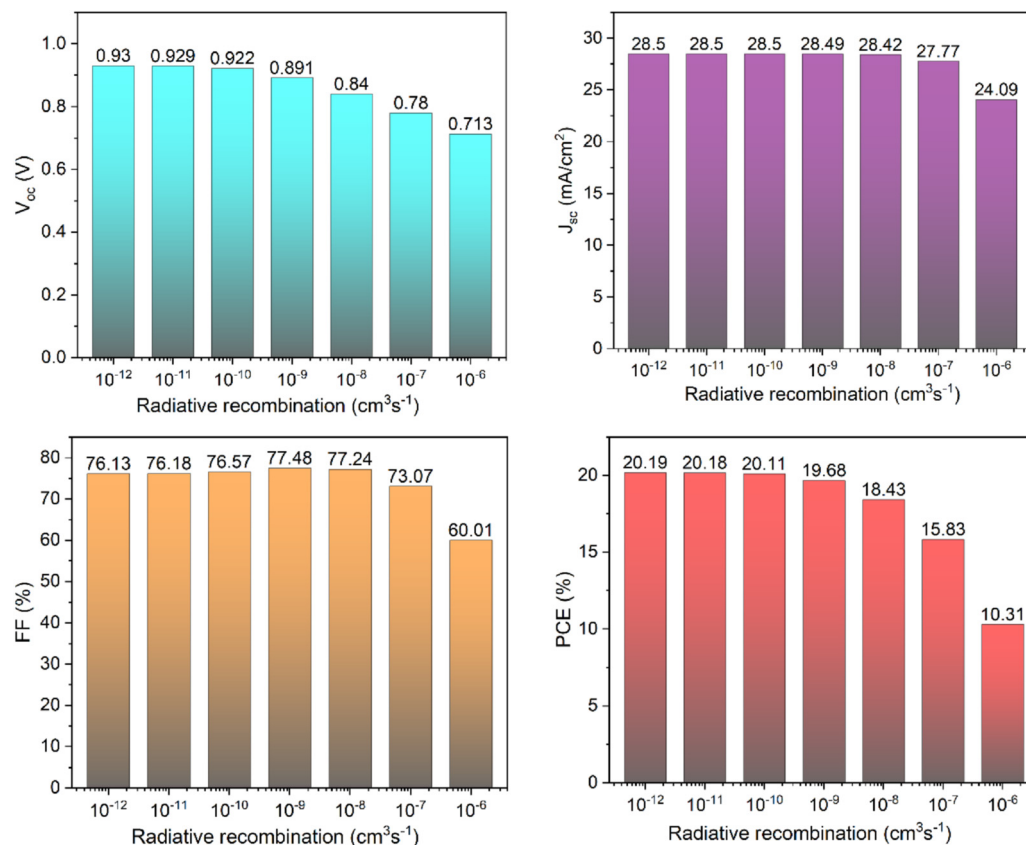**Fig. 12** Effects of reflection on PV outputs.

Fig. 13 Effects of radiative recombination on PV outputs.

HTL/absorber interfaces. As a result, the solar cell outputs reached V_{oc} = 0.93 V, J_{sc} = 31.73 mA cm^{-2}, FF = 83.75%, and PCE = 24.84%.

3.2.3. Effects of resistances on the proposed solar cell's outcomes. In the best of circumstances, parasitic resistances are disregarded. This section examines the impact of series (R_s) and shunt (R_{sh}) resistances after considering the effects of defects. The combined effect of the resistances from the connections across layers and the metal–semiconductor interfaces results in R_s.[70] As shown in Fig. 11, R_s varies from 0 to 5 Ω cm^2 and R_{sh} varies from 10 to 10^6 Ω cm^2. Because of the sharp decay in FF, the PCE drastically declined with significant R_s. J_{sc} shows a substantial reduction from 31.73 to 21.15 mA cm^{-2} due to increasing restriction for routing through layers with higher R_s. Hence, it is necessary to optimize R_s for maximizing device performance. Since it would lead to non-complementary absorption, cutting the absorber thickness during manufacture is not a workable way to minimize R_s.[71,72] On the other hand, a larger R_{sh} denotes less leakage over the junction because the thin layer is less prone to imperfections. Within the R_s range of 0–5 Ω cm^2, the PV parameters changed as follows: V_{oc} from 0.32 to 0.93 V, FF from 25 to 68.53%, and PCE from 2.52 to 20.35%, while J_{sc} remained unaltered at 31.73 mA cm^{-2} when R_{sh} was varied from 10 to 10^6 Ω cm^2. Under the optimized conditions of R_s = 2 Ω cm^2 and R_{sh} = 10^3 Ω cm^2, the solar cell outputs were as follows: 0.93 V (V_{oc}), 31.67 mA cm^{-2} (J_{sc}), 75.82% (FF), and 22.43% (PCE).

3.2.4. Effects of reflection on the proposed solar cell's outcomes. The capability of a photovoltaic device to capture incident photons is one of its essential features. Reflected light represents the portion of energy that the cell cannot utilize. Reflection and absorption losses can account for a significant portion of optical loss in solar cells.[73] Fig. 12 shows the change of the reflection parameter from 0% to 30% to incorporate the effect of optical loss in the form of reflectance. Higher reflection loss caused the PV parameters of the designed cell to deteriorate since the reflected light does not contribute to exciton generation. Hence, J_{sc} is drastically reduced from 31.67 to 22.17 mA cm^{-2}. V_{oc} is slightly decreased from 0.934 to 0.921 V, and as a result, PCE is further reduced from 22.43 to 15.62%. The average reflection is adjusted to 10%[74] in the FTO, and the obtained PV outputs are as follows: V_{oc} = 0.93 V, J_{sc} = 28.50 mA cm^{-2}, FF = 76.13%, and PCE = 20.19%. Nevertheless, anti-reflection coatings and surface texturing can be used to lower the reflection losses.

3.2.5. Effects of radiative recombination on the proposed solar cell's outcomes. In the development of highly efficient PSCs, recombination of charge carriers, whether radiative or non-radiative, is a prominent and detrimental challenge, and therefore, it must be reduced. Radiative recombination is a process in which an electron from the conduction band recombines with a hole in the valence band, emitting energy in the form of light with energy equal to the bandgap.[26]
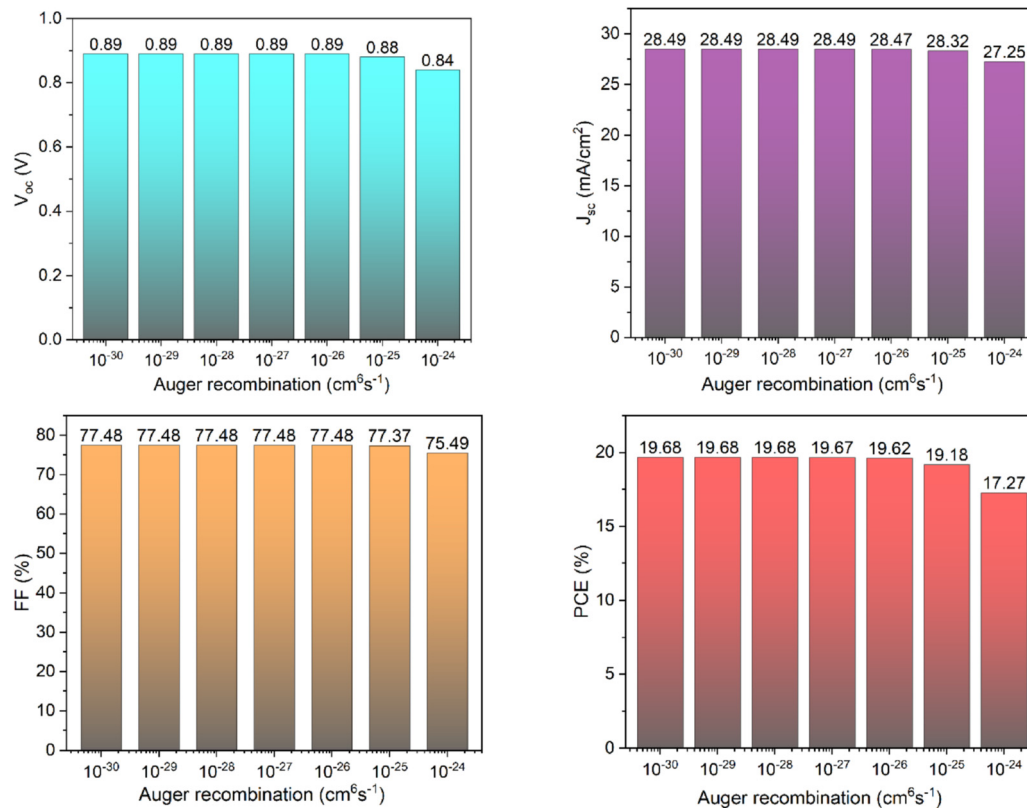
Fig. 14 Effects of Auger recombination on PV outputs.

Mathematically, the radiative recombination coefficient can be expressed using the following equation:[25]

$$B_r = \frac{1}{\tau_{n,rad} \text{ or } \tau_{p,rad} \times N_A \text{ or } N_D},$$ (4)

where $\tau_{n,rad}$ and $\tau_{p,rad}$ are the electron minority and hole carrier radiative lifetime, and N_D and N_A stand for the donor and acceptor densities, respectively. Furthermore, the carrier lifetime can be expressed as follows:[32]

$$\tau_{n \text{ or } p,rad} = \frac{1}{\sigma_{n,p} N_t V_{th}},$$ (5)

where $\sigma_{n,p}$ is the capture cross-section of electrons and holes, V_{th} is the thermal velocity of charge carriers and N_t is the defect density of the absorber.

In this numerical study, the rate of radiative recombination is varied between 10^{-12} and 10^{-6} cm^3 s^{-1}, and the corresponding influence on the PV performance metrics is demonstrated in Fig. 13. From the figure, it is evident that, when the radiative recombination increases, the PV performance parameters, including V_{oc}, J_{sc}, FF, and PCE, decrease significantly. As the radiative recombination rate increases from 10^{-12} to 10^{-6} cm^3 s^{-1}, the values of V_{oc}, J_{sc}, FF, and PCE decline from 0.93 to 0.713 V, 28.5 to 24.09 mA cm^{-2}, 76.13% to 60.01%, and 20.19% to 10.31%, respectively. In our investigation, we selected a radiative recombination rate of 10^{-9} cm^3 s^{-1}, which closely aligns with the published reports.[75,76]

3.2.6. Effects of Auger recombination on the proposed solar cell's outcomes. In addition to radiative recombination, non-radiative recombination, such as Auger recombination,

Table 4 Performance comparison of various algorithms

Model	MSE	MAE	RMSE	R^2	CV R^2	CV RMSE
RF	0.0249	0.1048	0.1579	0.9994	0.9988 ($\pm$0.0003)	0.2126
GBR	0.0049	0.0489	0.0698	0.9999	0.9998 ($\pm$0.0001)	0.0894
SVR	19.5550	2.7430	4.4221	0.5085	0.5457 ($\pm$0.0235)	4.2364
XGBoost	0.0035	0.0431	0.0591	0.9999	0.9998 ($\pm$0.0001)	0.0794
MLP	13.0723	2.7828	3.6156	0.6714	0.6789 ($\pm$0.0119)	3.5589
LightGBM	0.0094	0.0692	0.0969	0.9998	0.9997 ($\pm$0.0001)	0.1055
CatBoost	0.0028	0.0345	0.0525	0.9999	0.9997 ($\pm$0.0002)	0.1087
ANN	12.4935	2.6414	3.5346	0.6860	0.6446 ($\pm$0.0916)	3.7061
DNN	12.3756	2.6875	3.5179	0.6889	0.6856 ($\pm$0.0231)	3.5174
CNN	12.7929	2.7597	3.5767	0.6784	0.6934 ($\pm$0.0270)	3.4700
LSTM	11.9763	2.5919	3.4607	0.6990	0.5529 ($\pm$0.2114)	4.0927

Fig. 15   (a–g) Test parity plots of various ML algorithms.

also impacts the performance of the designed PSCs.[77] Auger recombination is a non-radiative phenomenon in which the energy released by the recombination of an electron–hole pair is transmitted to a third carrier, which is excited to a higher energy state rather than contributing to the photon emission.[77]

Mathematically, the Auger recombination coefficient can be expressed using the following equation:[25]

$$B_{\text{Auger,n}} \text{ or } B_{\text{Auger,p}} = \frac{1}{\tau_{\text{Auger,n}} \text{ or } \tau_{\text{Auger,p}} \times N_{\text{A}}^2 \text{ or } N_{\text{D}}^2}, \quad (6)$$

(a) (b)

(c) (d)

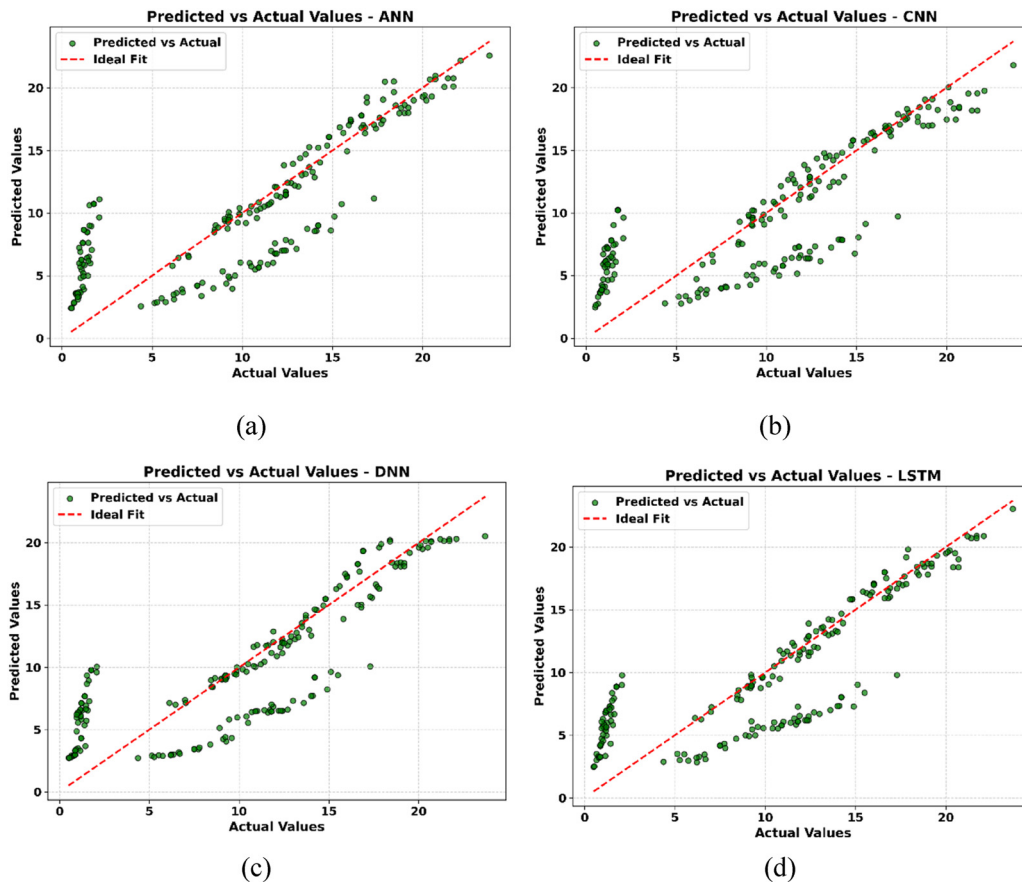**Fig. 16** (a–d) Test parity plots of various DL algorithms.

Table 5 Summary of the hyperparameters of the optimized XGBoost model

Hyperparameters	Values
learning_rate	0.1
max_depth	6
n_estimators	300
subsample	0.8

Fig. 17 SHAP summary bar plot showing feature contributions to the XGBoost model prediction.

where $B_{Auger,n}$ and $B_{Auger,p}$ are the electron and hole Auger recombination coefficients, $\tau_{Auger,n}$ and $\tau_{Auger,p}$ represent the electron and hole carrier Auger lifetimes, and N_D and N_A stand for the donor and acceptor densities, respectively. Furthermore, the electron and hole carrier Auger lifetimes can be calculated using eqn (5).

The variation of the Auger recombination rate of the proposed structure and its effects on the PV performance parameters are illustrated in Fig. 14. It can be observed from the figure that, when the Auger recombination rate increases from 10^{-30} to 10^{-24} cm^6 s^{-1}, the performance metrics of the designed PSC decrease gradually: the values of V_{oc}, J_{sc}, FF, and PCE decrease from 0.89 to 0.84 V, 28.49 to 27.25 mA cm^{-2}, 77.48% to 75.49%, and 19.68% to 19.18%, respectively. In this theoretical investigation, we select an Auger recombination rate of 10^{-29} cm^6 s^{-1}, which closely aligns with the published reports.[75,76]

3.3. Prediction of solar cell efficiency using various machine and deep learning algorithms

In this study, seven ML and four DL models were used to predict solar cell efficiency based on five non-ideal input features. These models were selected for their ability to model non-linear relationships and perform effectively on moderate-sized datasets. The combination of these ML and DL models allows for a comprehensive evaluation of predictive performance in modeling solar cell behavior.

3.3.1. Comparative analysis and performance evaluation of various algorithms. In this section, a comparison is made among the seven ML and four DL models to evaluate their
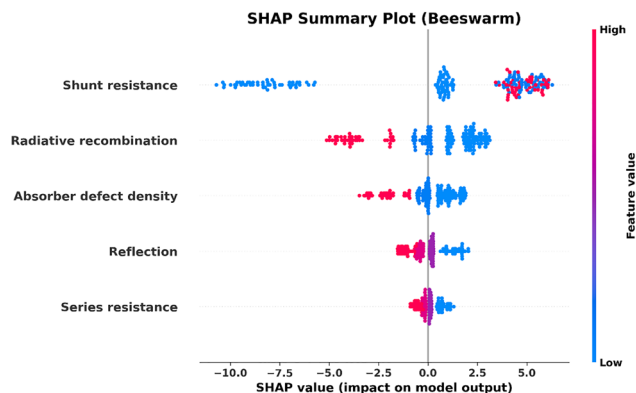
Fig. 18 SHAP beeswarm plot showing feature contributions to the XGBoost model prediction.
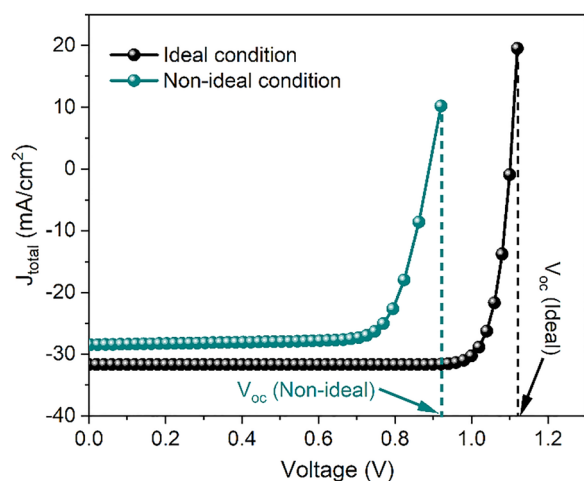

Fig. 19 J–V characteristics of the RbGeI$_3$-based PSC under ideal and non-ideal conditions.

effectiveness in predicting solar cell efficiency. The performance metrics, including the 5-fold cross-validation scores, are detailed in Table 4. The test parity plots for the ML and DL models are displayed in Fig. 15 and 16, respectively. Among the ML models, XGBoost, CatBoost, and GBR achieved

near-perfect predictive accuracy, with XGBoost leading the group with a test R^2 of 0.9999 and a test RMSE of 0.0591. The 5-fold cross-validation R^2 for XGBoost (0.9998 $\pm$ 0.0001) provides a rigorous confirmation that the model is not overfitting to the SCAPS-generated data but has successfully captured the underlying patterns. In contrast, the SVR model shows significantly higher error values, with a test MSE of 19.5550 and a lower R^2 of only 0.5085, indicating a poor fit to the data and limited ability to model the underlying relationships. Interestingly, while the deep learning models (ANN, DNN, CNN, and LSTM) were able to learn general trends, their performance was significantly lower than that of the ensemble tree-based models, achieving R^2 values ranging only between 0.6784 and 0.6990. While the smaller size of the dataset (1024 samples) is a contributing factor, the relatively low dimensionality of the input features (consisting of only five features) favors the partitioning logic of ensemble tree methods over the high-parameter DL architectures. Deep learning models typically work well in high-dimensional spaces, where they can extract hierarchical features. However, for this shallow feature space, tree-based models like XGBoost provide a more efficient mathematical mapping. Overall, the consistent results between the test metrics and the cross-validation scores confirm that gradient-boosting models are the most robust and suitable choice for solar cell performance prediction.

3.3.2. Proposed XGBoost model. The proposed extreme gradient boosting (XGBoost) model demonstrated superior predictive performance across all key evaluation metrics, making it the most effective algorithm among the models explored for predicting solar cell efficiency. XGBoost was selected due to its robust ability to capture complex non-linear interactions between input variables and the output target, its built-in regularization mechanisms, and its efficiency in training and prediction, particularly with structured tabular data. The XGBoost model operates by constructing an ensemble of decision trees in a sequential manner, where each subsequent tree attempts to correct the errors made by its predecessor. Additionally, XGBoost incorporates L1 and L2 regularization, which helps prevent overfitting—a critical feature when working with small to moderate datasets like the one used in this study.

The optimal configuration of the XGBoost model was determined through manual grid search, and the selected

Table 6 Physical parameters optimized for the proposed RbGeI$_3$ PV device

Optimized parameters (unit)	ZnO ETL	RbGeI$_3$ absorber	Cu$_2$O HTL	Interface defect density		Resistance	Reflection
				RbGeI$_3$/ZnO	Cu$_2$O/RbGeI$_3$		
Thickness (μm)	0.05	1.0	0.1				
N_D (cm^{-3})	10^{18}	1.0×10^9	—				
N_A (cm^{-3})	—	1.0×10^9	10^{18}				
N_t (cm^{-3})	10^{15}	10^{14}	10^{15}				
Total density (cm^{-2})				10^{14}	10^{14}		
B_r (cm^3 s^{-1})	10^{-9}	10^{-9}	10^{-9}				
$B_{Auger,p}$ (cm^6 s^{-1})	10^{-29}	10^{-29}	10^{-29}				
$B_{Auger,p}$ (cm^6 s^{-1})	10^{-29}	10^{-29}	10^{-29}				
R_s (Ω cm^2)						2.0	
R_{sh} (Ω cm^2)						10^3	
R (%)							10

Table 7 Summary of the PV parameters of the RbGeI$_3$-based PSC under ideal and non-ideal conditions

Steps	V_{oc} (V)	J_{sc} (mA cm^{-2})	FF (%)	Efficiency (%)
Ideal conditions	1.10	31.73	87.04	30.41
Applying absorber bulk defect density	0.96	31.73	81.89	25.00
Applying defect density at both interfaces	0.93	31.73	83.75	24.84
Applying resistances	0.93	31.67	75.82	22.43
Applying reflection losses	0.93	28.50	76.13	20.19
Applying radiative recombination	0.89	28.49	77.48	19.68
Applying Auger recombination	0.89	28.49	77.48	19.68

hyperparameters are summarized in Table 5. The model was trained with a learning rate of 0.1, a maximum tree depth of 6, and 300 estimators, ensuring both speed and accuracy in convergence. A subsample ratio of 0.8 was used to enhance model generalization by introducing randomness during training. These hyperparameter choices provided a balance between complexity and bias–variance trade-off. The proposed XGBoost model achieved outstanding results, with a test MSE of 0.0035, RMSE of 0.0592, MAE of 0.0431, an R^2 score of 0.9999, a cross validation (CV) R^2 score of 0.9998 ($\pm$0.0001) and a CV RMSE of 0.0794, indicating its exceptional ability to predict solar cell performance with minimal error, and also there is no sign of overfitting. These outcomes confirm that the XGBoost algorithm is highly reliable for capturing the non-linear dependencies between the non-ideal parameters and their impact on overall solar cell efficiency.

3.3.3. Feature significance with Shapley additive explanations (SHAP).
SHAP is employed to thoroughly interpret the predictions of the XGBoost algorithm by quantifying the contribution of each input feature to the model's output.[78] SHAP values indicate how individual features affect specific predictions—positive values suggest an increase in the predicted output, while negative values indicate a decrease. This approach helps identify which features consistently drive the model's predictions and to what extent, offering valuable insight into the model's decision-making process. Two types of SHAP visualizations were utilized: the summary bar plot (Fig. 17), which ranks features by average importance, and the beeswarm plot (Fig. 18), which provides a detailed view of how

feature values affect predictions across samples. As shown in the SHAP summary bar plot (Fig. 17), shunt resistance emerged as the most influential feature in determining the model's predictions, followed by radiative recombination, absorber defect density, reflection, and series resistance. This ranking reflects the average magnitude of each feature's impact on model outputs. The beeswarm plot (Fig. 18) further reveals that high values of shunt resistance are associated with higher predicted efficiency (positive SHAP values), while lower shunt resistance values negatively influence efficiency. On the other hand, high values of radiative recombination and absorber defect density tend to reduce efficiency, consistent with physical expectations in photovoltaic behavior.

3.4. Overall performance of the final RbGeI$_3$-based PSC

The J–V characteristics of the proposed solar cell structure under ideal and experimentally motivated non-ideal conditions are illustrated in Fig. 19. From the figure, it is observed that the values of V_{oc} and J_{sc} decrease from 1.10 to 0.89 V and 31.73 to 28.49 mA cm^{-2}, when non-ideal parameters are included in the designed PV device. Additionally, the physical parameters optimized for the proposed structure are listed in Table 6. These optimized parameters show excellent agreement with the parameters obtained experimentally. The overview of the PV performance metrics of the designed RbGeI$_3$-based PSC under ideal and non-ideal conditions is shown in Table 7. It can be seen that for individual non-ideal parameters, the PV performance metrics decrease gradually. For the introduction of bulk defect density, the power conversion efficiency reduces from 30.41% to 25%, indicating that bulk recombination is a major contributor to performance degradation. Upon incorporating the remaining five non-ideal parameters (e.g., interface defects, series resistance, shunt resistance, reflection, radiative, and Auger recombination losses), the efficiency further decreases from 25% to 19.68%. This analysis demonstrates that bulk defect density accounts for the largest individual efficiency drop (5.41%), while the combined effect of the other five experimentally motivated non-ideal factors contributes an additional reduction of 5.32%. Therefore, bulk recombination emerges as the single most dominant degradation mechanism, whereas the remaining losses arise from the cumulative impact of interfacial, resistive, reflection, and recombination effects.

Table 8 Comparison of PV outputs obtained for various RbGeI$_3$-based PSC devices

Structures	Research area	Efficiency (%)	Ref.
FTO/TiO$_2$/RbGeI$_3$/Ag	Theoretical	3.60	79
FTO/TiO$_2$/RbGeI$_3$/NiO/Ag	—	10.11	10
TCO/TiO$_2$/RbGeI$_3$/CuSCN/Ag	—	12.57	10
FTO/IDL1/RbGeI$_3$/IDL2	—	17.78	15
FTO/ZnSe/RbGeI$_3$/CuSCN/Au	—	17.93	16
FTO/TiO$_2$/RbGeI$_3$/CuI/Ag	—	18.10	7
FTO/PCBM/RbGeI$_3$/PTAA/C	—	21.89	80
FTO/TiO$_2$/RbGeI$_3$/PTAA/Au	—	24.03	9
ITO/TiO$_2$/RbGeI$_3$/Sb$_2$S$_3$/Pt	—	30.35	6
FTO/ZnO/RbGeI$_3$/Cu$_2$O/Ni (ideal conditions)	—	30.41	This work
FTO/ZnO/RbGeI$_3$/Cu$_2$O/Ni (non-ideal conditions)	—	19.68	This work

© 2026 The Author(s). Published by the Royal Society of Chemistry

The configuration of RbGeI$_3$-based PSCs designed by various research groups is listed in Table 8. According to the table, although experimental investigations have not yet been performed on RbGeI$_3$-based solar cells, many research groups have identified the potential of RbGeI$_3$-based materials in solar cell technology. Theoretically, the efficiency of the RbGeI$_3$-based PV devices increases from 3.60% to 30.35%.[6,7,9,10,15,16,79,80] In our work, we obtained the highest PCE of 30.41%, considering the ideal conditions. On the other hand, when we introduced experimentally motivated non-ideal conditions, the PCE reduced to 19.68%, which shows good agreement with the experimental outcomes of the PSCs.[81,82] Therefore, it can serve as a benchmark and guide for future research and may assist experimental scientists in designing and optimizing similar device structures. Additionally, various ML and DL models are employed to predict the efficiency of the proposed PSC and to evaluate the influence of individual non-ideal parameters on device performance. The complete
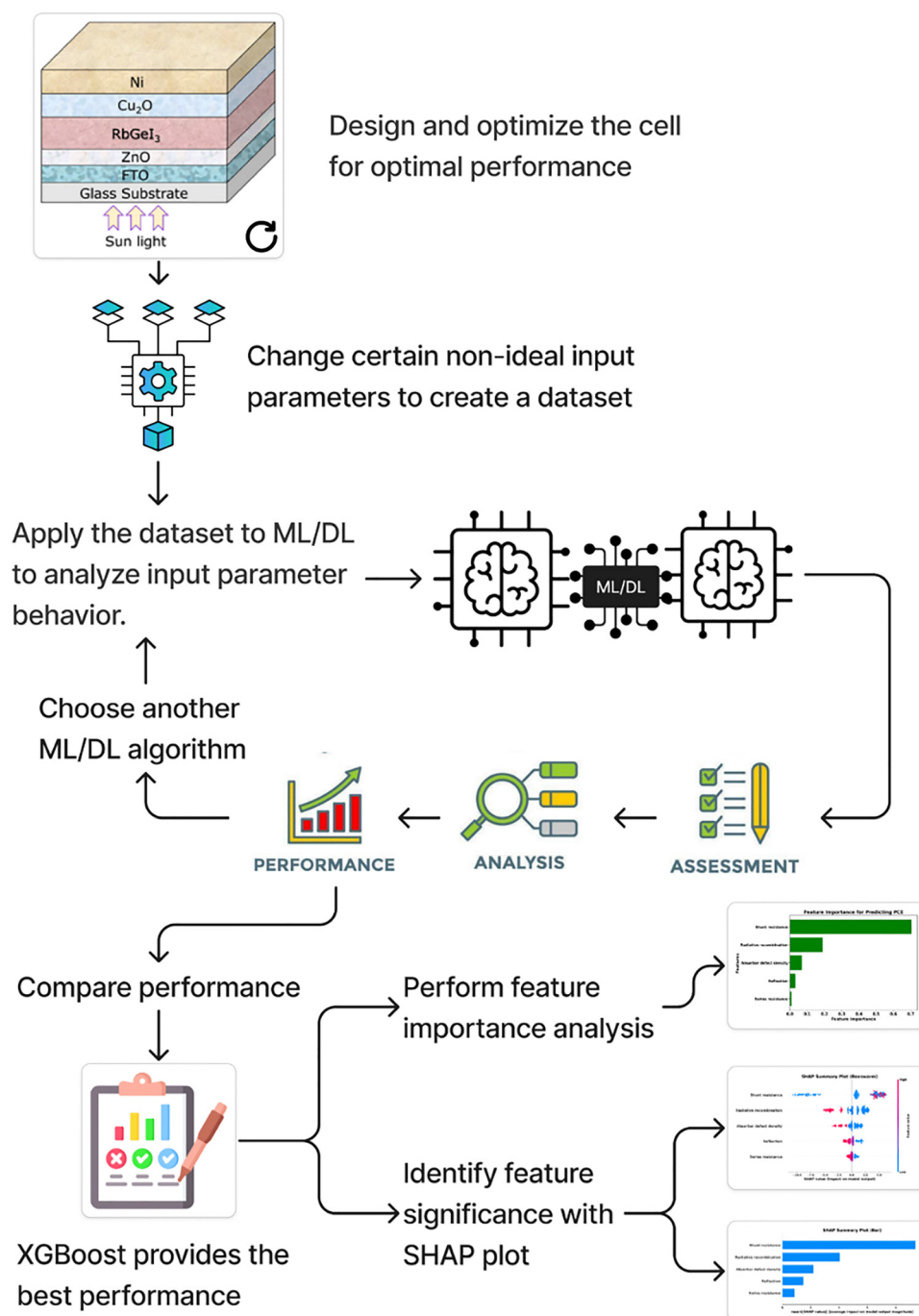

Fig. 20 Graphical illustration of the application of various ML and DL algorithms for predicting the efficiency of the proposed PSC.

workflow—from dataset generation to final model optimization—is illustrated in Fig. 20.

4. Conclusion

In this study, a lead-free planar heterostructure $RbGeI_3$-based PSC is designed and examined using the SCAPS-1D simulator. The performance of the proposed $FTO/ZnO/RbGeI_3/Cu_2O/Ni$ structure is analyzed under ideal and experimentally motivated non-ideal conditions. To achieve the maximum PCE of 30.41% with a V_{oc} of 1.10 V, a J_{sc} of 31.73 mA cm^{-2}, and an FF of 87.04%, the thickness and carrier concentration of various layers are optimized. Here, the thicknesses of the $RbGeI_3$ perovskite layer, the ZnO ETL, and the Cu_2O HTL are selected as 1.0 μm, 0.05 μm, and 0.1 μm, respectively. Additionally, the carrier concentration of the ZnO ETL and the Cu_2O HTL is selected as 10^{18} cm^{-3}. Later, we have introduced various non-ideal parameters, including defect density at bulk and interfaces, parasitic resistance (series and shunt), reflection losses, and radiative and Auger recombination losses, and attained a PCE of 19.68% with a V_{oc} of 0.89 V, a J_{sc} of 28.49 mA cm^{-2}, and an FF of 77.48%. Despite the device's performance diminishing significantly, it still holds substantial importance to experimental researchers. Later, we have employed seven ML and four DL algorithms to determine the most efficient algorithm for performance prediction in solar cell technology. Among the eleven algorithms, XGBoost performs outstandingly with an excellent R^2 value of 0.9999 and a lower MSE value of 0.0038. Besides, the SHAP plot is used to illustrate the effect of each non-ideal parameter on the PCE of the designed structure, and it is observed that shunt resistance prevails among them. In general, despite the performance of PV devices declining substantially, this study emphasizes the significance of non-idealities in PV technology in bridging the gap between idealized simulations and practical device characteristics. While the present work is purely simulation-based and does not include experimental validation, it provides theoretical insights into the performance limits and sensitivity of lead-free $RbGeI_3$-based perovskite solar cells to various non-ideal factors. Moreover, these findings are intended to serve as a guiding framework for future experimental investigations rather than a direct demonstration of immediate fabrication feasibility.

Conflicts of interest

There are no conflicts to declare.

Data availability

The dataset generated and analysed during this study is available at: https://github.com/TM-Khan-9/RbGeI3-perovskite-solar-cell/blob/RbGeI3-perovskite-solar-cell/RbGeI3%20ML%20PCE.xlsx, while the Notebook containing the full modelling and analysis code is available at: https://github.com/TM-Khan-9/RbGeI3-perovskite-solar-cell/blob/RbGeI3-perovskite-solar-cell/solar3.

ipynb. All materials are openly accessible through the GitHub repository.

References

1 M. K. Hossain, A. Arnab, R. C. Das, K. Hossain, M. Rubel, M. F. Rahman, H. Bencherif, M. Emetere, M. K. Mohammed and R. Pandey, Combined DFT, SCAPS-1D, and wxAMPS frameworks for design optimization of efficient Cs_2BiAgI_6-based perovskite solar cells with different charge transport layers, *RSC Adv.*, 2022, **12**, 35002–35025.

2 A. Kuddus, M. F. Rahman, J. Hossain and A. B. M. Ismail, Enhancement of the performance of CdS/CdTe heterojunction solar cell using TiO_2/ZnO bi-layer ARC and V_2O_5 BSF layers: a simulation approach, *Eur. Phys. J. Appl. Phys.*, 2020, **92**, 20901.

3 M. M. Lee, J. Teuscher, T. Miyasaka, T. N. Murakami and H. J. Snaith, Efficient Hybrid Solar Cells Based on Meso-Superstructured Organometal Halide Perovskites, *Science*, 2012, **338**, 643–647.

4 S. S. Bal, A. Basak and U. P. Singh, Numerical modeling and performance analysis of Sb-based tandem solar cell structure using SCAPS–1D, *Opt. Mater.*, 2022, **127**, 112282.

5 Y. Yu, N. Zhang and J. D. Kim, Impact of urbanization on energy demand: An empirical study of the Yangtze River Economic Belt in China, *Energy Policy*, 2020, **139**, 111354.

6 M. M. Rahman, M. H. Ali, M. D. Haque and A. Z. M. T. Islam, Numerical modeling and extensive analysis of an extremely efficient $RbGeI_3$-based perovskite solar cell by incorporating a variety of ETL and HTL materials to enhance PV performance, *Energy Adv.*, 2024, **3**, 2377–2398.

7 S. Samaki, F. Tchangnwa Nya, G. M. Dzifack Kenfack and A. Laref, Materials and interfaces properties optimization for high-efficient and more stable $RbGeI_3$ perovskite solar cells: optoelectrical modelling, *Sci. Rep.*, 2023, **13**, 15517.

8 I. Hanif, S. M. F. Raza, P. Gago-de-Santos and Q. Abbas, Fossil fuels, foreign direct investment, and economic growth have triggered CO_2 emissions in emerging Asian economies: some empirical evidence, *Energy*, 2019, **171**, 493–501.

9 B. K. Ravidas, A. R. Kumar, A. Praveen, S. K. Agnihotri, S. Bhattarai, R. Pandey, J. Madan, S. Singh, M. K. Hossain and M. K. Roy, Integration of SCAPS-1D and density functional theory for the performance evaluation of $RbGeI_3$-based perovskite solar cell, *J. Phys. Chem. Solids*, 2025, **196**, 112325.

10 G. Pindolia, S. M. Shinde and P. K. Jha, Optimization of an inorganic lead free RbGeI$_3$ based perovskite solar cell by SCAPS-1D simulation, *Sol. Energy*, 2022, **236**, 802–821.

11 R. Gopal, V. Narayanan, D. K. Dhaked and A. Gupta, Performance enhancement of inorganic Cs$_2$AgInBr$_6$-based perovskite solar cell by numerical simulation, *J. Phys. Chem. Solids*, 2024, **193**, 112184.

12 H. Beck, C. Gehrmann and D. A. Egger, Structure and binding in halide perovskites: Analysis of static and dynamic effects from dispersion-corrected density functional theory, *APL Mater.*, 2019, **7**, 021108.

13 K. D. Jayan and V. Sebastian, Ab initio DFT determination of structural, mechanical, optoelectronic, thermoelectric and thermodynamic properties of RbGeI$_3$ inorganic perovskite for different exchange-correlation functionals, *Mater. Today Commun.*, 2021, **28**, 102650.

14 Z.-L. Yu, Q.-R. Ma, B. Liu, Y.-Q. Zhao, L.-Z. Wang, H. Zhou and M.-Q. Cai, Oriented tuning the photovoltaic properties of γ-RbGeX$_3$ by strain-induced electron effective mass mutation, *J. Phys. D: Appl. Phys.*, 2017, **50**, 465101.

15 Z. Qin, Y. Zhang and J. Guo, SCAPS simulation and DFT study of ultra-thin lead-free perovskite solar cells based on RbGeI$_3$, *Opt. Commun.*, 2024, **554**, 130187.

16 A. Talukdar, P. Debnath, J. Sarkar and S. Chatterjee, Unveiling the role of band offset in inorganic RbGeI$_3$-based perovskite solar cells: a numerical study in SCAPS-1D, *Indian J. Phys.*, 2024, **98**, 3913–3929.

17 W. Ke and M. G. Kanatzidis, Prospects for low-toxicity lead-free perovskite solar cells, *Nat. Commun.*, 2019, **10**, 965.

18 N. K. Noel, S. D. Stranks, A. Abate, C. Wehrenfennig, S. Guarnera, A.-A. Haghighirad, A. Sadhanala, G. E. Eperon, S. K. Pathak and M. B. Johnston, Lead-free organic–inorganic tin halide perovskites for photovoltaic applications, *Energy Environ. Sci.*, 2014, **7**, 3061–3068.

19 G. Thiele, H. Rotter and K. Schmidt, Die Kristallstrukturen und phasentransformationen des tetramorphen RbGeI$_3$, *Z. Anorg. Allg. Chem.*, 1989, **571**, 60–68.

20 K. A. Parrey, T. Farooq, S. A. Khandy, U. Farooq and A. Gupta, First principle studies on structure, magneto-electronic and elastic properties of photovoltaic semiconductor halide (RbGeI$_3$) and ferromagnetic half metal oxide (RbDyO$_3$), *Comput. Condens. Matter*, 2019, **19**, e00381.

21 U.-G. Jong, C.-J. Yu, Y.-H. Kye, Y.-G. Choe, W. Hao and S. Li, First-principles study on structural, electronic, and optical properties of inorganic Ge-based halide perovskites, *Inorg. Chem.*, 2019, **58**, 4134–4140.

22 S. Rühle, Tabulated values of the Shockley–Queisser limit for single junction solar cells, *Sol. Energy*, 2016, **130**, 139–147.

23 D. Sarkar, M. Mottakin, A. M. Hasan, V. Selvanathan, K. Sobayel, M. Khan, A. M. Rabbani, M. Shahinuzzaman, M. Aminuzzaman and F. H. Anuar, A comprehensive study on RbGeI$_3$ based inorganic perovskite solar cell using green synthesized CuCrO$_2$ as hole conductor, *J. Photochem. Photobiol., A*, 2023, **439**, 114623.

24 M. Panachikkool, E. Aparna and T. Pandiyarajan, Numerical modelling of CuBi$_2$O$_4$ thin film solar cells with SCAPS-1D: Bridging the gap ideal and non-ideal conditions, *Mater. Lett.*, 2024, **367**, 136590.

25 S. Chowdhury, A. S. Najm, M. Luengchavanon, A. M. Holi, C. H. Chia, K. Techato, S. Channumsin and I. K. Salih, Investigating the effect of nonideal conditions on the performance of a planar Sb$_2$Se$_3$-based solar cell through SCAPS-1D simulation, *Energy Fuels*, 2023, **37**, 6722–6732.

26 S. R. Hosseini, M. Bahramgour, P. Y. Sefidi, A. T. Mashayekh, A. Moradi, N. Delibas, M. G. Hosseini and A. Niaei, Investigating the effect of non-ideal conditions on the performance of a planar CH$_3$NH$_3$PbI$_3$-based perovskite solar cell through SCAPS-1D simulation, *Heliyon*, 2022, **8**, e11471.

27 M. Panachikkool, E. Aparna, P. Asaithambi and T. Pandiyarajan, Design and numerical simulation of CuBi$_2$O$_4$ solar cells with graphene quantum dots as hole transport layer under ideal and non-ideal conditions, *Sci. Rep.*, 2025, **15**, 100.

28 T. M. Khan, B. Islam, M. M. Rahaman, M. M. Shakil, M. F. Rahman and S. R. Al Ahmed, Predictive design and performance analysis of lead-free CH$_3$NH$_3$SnI$_3$-based perovskite solar cells through a combination of SCAPS-1D and machine learning based modelling, *Sol. Energy Mater. Sol. Cells*, 2025, **282**, 113388.

29 D. R. Ahmed and F. F. Muhammadsharif, A Review of Machine Learning in Organic Solar Cells, *Processes*, 2025, **13**, 393.

30 A. Mahmood, A. Irfan and J.-L. Wang, Machine learning for organic photovoltaic polymers: a minireview, *Chin. J. Polym. Sci.*, 2022, **40**, 870–876.

31 H. Togun, A. Basem, M. J. Jweeg, N. Biswas, A. M. Abed, D. Paul, H. I. Mohammed, A. Chattopadhyay, B. K. Sharma and T. Abdulrazzaq, Advancing organic photovoltaic cells for a sustainable future: The role of artificial intelligence (AI) and deep learning (DL) in enhancing performance and innovation, *Sol. Energy*, 2025, **291**, 113378.

32 T. M. Khan, A. Hosen, O. Saidani and S. R. Al Ahmed, Artificial neural network assisted numerical analysis on performance enhancement of Sb$_2$(S,Se)$_3$ solar cell with SnS as HTL, *Mater. Today Commun.*, 2024, **40**, 109639.

33 M. S. Islam, M. T. Islam, S. Sarker, H. A. Jame, S. S. Nishat, M. R. Jani, A. Rauf, S. Ahsan, K. M. Shorowordi and H. Efstathiadis, Machine learning approach to delineate the impact of material properties on solar cell device physics, *ACS Omega*, 2022, **7**, 22263–22278.

34 R. Kundara and S. Baghel, Predictive design of KSnI$_3$-based perovskite solar cells using SCAPS and machine learning model, *Mater. Sci. Eng., B*, 2024, **307**, 117536.

35 T. M. Khan, O. Saidani and S. R. Al Ahmed, Utilizing machine learning to enhance performance of thin-film solar cells based on Sb$_2$(S$_x$Se$_{1-x}$)$_3$: investigating the influence of material properties, *RSC Adv.*, 2024, **14**, 27749–27763.

36 I. O. Oboh, U. H. Offor and N. D. Okon, Artificial neural network modeling for potential performance enhancement

of a planar perovskite solar cell with a novel TiO_2/SnO_2 electron transport bilayer using nonlinear programming, *Energy Rep.*, 2022, **8**, 973–988.

37 N. Kaur, R. Pandey, M. K. Hossain and J. Madan, Machine learning-aided optimization for transport layer parameters of low lead inorganic Zn-based mixed-halide perovskite solar cell, *Sol. Energy*, 2023, **264**, 112055.

38 T. M. Khan, B. Islam and S. R. Al Ahmed, Performance analysis and optimization of SnSe thin-film solar cell with Cu_2O HTL through a combination of SCAPS-1D and machine learning approaches, *Mater. Today Commun.*, 2024, **41**, 110490.

39 M. Burgelman, P. Nollet and S. Degrave, Modelling poly-crystalline semiconductor solar cells, *Thin Solid Films*, 2000, **361**, 527–532.

40 S. Marimuthu, S. Shriswaroop, M. Muthumareeswaran, S. Pandiaraj, A. N. Alodhayb, T. A. Alrebdi and A. N. Grace, Drift diffusion modelling of cell parameters effect on the performance of perovskite solar cells with MXene as additives, *Sol. Energy*, 2023, **262**, 111804.

41 Materials Data on $RbGeI_3$ by Materials Project, *Mater. Project*, 2020.

42 F. Wang, S. Bai, W. Tress, A. Hagfeldt and F. Gao, Defects engineering for high-performance perovskite solar cells, npj Flex, *Electron.*, 2018, **2**, 22.

43 J. Siekmann, S. Ravishankar and T. Kirchartz, Apparent defect densities in halide perovskite thin films and single crystals, *ACS Energy Lett.*, 2021, **6**, 3244–3251.

44 Z. Ni, C. Bao, Y. Liu, Q. Jiang, W.-Q. Wu, S. Chen, X. Dai, B. Chen, B. Hartweg and Z. Yu, Resolving spatial and energetic distributions of trap states in metal halide perovskite solar cells, *Science*, 2020, **367**, 1352–1358.

45 J. T. Ryan, A. Matsuda, J. P. Campbell and K. P. Cheung, Interface-state capture cross section—Why does it vary so much?, *Appl. Phys. Lett.*, 2015, **106**, 163503.

46 M. Matys, R. Stoklas, J. Kuzmik, B. Adamowicz, Z. Yatabe and T. Hashizume, Characterization of capture cross sections of interface states in dielectric/III-nitride heterojunction structures, *J. Appl. Phys.*, 2016, **119**, 205304.

47 D. Tsikritzis, K. Chatzimanolis, N. Tzoganakis, S. Bellani, M. I. Zappia, G. Bianca, N. Curreli, J. Buha, I. Kriegel and N. Antonatos, Two-dimensional BiTeI as a novel perovskite additive for printable perovskite solar cells, *Sustainable Energy Fuels*, 2022, **6**, 5345–5359.

48 S. Z. Haider, H. Anwar, Y. Jamil and M. Shahid, A comparative study of interface engineering with different hole transport materials for high-performance perovskite solar cells, *J. Phys. Chem. Solids*, 2020, **136**, 109147.

49 D. N. Q. Agha and Q. T. Algwari, The influence of the conduction band engineering on the perovskite solar cell performance, *Results Opt.*, 2022, **9**, 100291.

50 Y. Raoui, H. Ez-Zahraouy, N. Tahiri, O. El Bounagui, S. Ahmad and S. Kazim, Performance analysis of $MAPbI_3$ based perovskite solar cells employing diverse charge selective contacts: Simulation study, *Sol. Energy*, 2019, **193**, 948–955.

51 N. Kumari, S. R. Patel and J. V. Gohel, Enhanced stability and efficiency of Sn containing perovskite solar cell with $SnCl_2$ and SnI_2 precursors, *J. Mater. Sci.: Mater. Electron.*, 2018, **29**, 18144–18150.

52 X. Qu and X. Sun, Impedance spectroscopy for quantum dot light-emitting diodes, *J. Semicond.*, 2023, **44**, 091603.

53 K. Sekar, L. Marasamy, S. Mayarambakam and P. Selvarajan, J. Bouclé, Highly efficient lead-free silver bismuth iodide (Ag_3BiI_6) rudorffite solar cells with novel device architecture: a numerical study, *Mater. Today Commun.*, 2024, **38**, 108347.

54 T. Minemoto, T. Matsui, H. Takakura, Y. Hamakawa, T. Negami, Y. Hashimoto, T. Uenoyama and M. Kitagawa, Theoretical analysis of the effect of conduction band offset of window/CIS layers on performance of CIS solar cells using device simulation, *Sol. Energy Mater. Sol. Cells*, 2001, **67**, 83–88.

55 S. Al-Dahidi, M. Alrbai, H. Alahmer, B. Rinchi and A. Alahmer, Enhancing solar photovoltaic energy production prediction using diverse machine learning models tuned with the chimp optimization algorithm, *Sci. Rep.*, 2024, **14**, 18583.

56 N. E. Benti, M. D. Chaka and A. G. Semie, Forecasting renewable energy generation with machine learning and deep learning: Current advances and future prospects, *Sustain.*, 2023, **15**, 7087.

57 Y. Xu and R. Goodacre, On splitting training and validation set: a comparative study of cross-validation, bootstrap and systematic sampling for estimating the generalization performance of supervised learning, *J. Anal. Test*, 2018, **2**, 249–262.

58 K. M. Sujon, R. B. Hassan, Z. T. Towshi, M. A. Othman, M. A. Samad and K. Choi, When to Use Standardization and Normalization: Empirical Evidence from Machine Learning Models and XAI, *IEEE Access*, 2024, **12**, 135300–135314.

59 H. Alibrahim and S. A. Ludwig, Hyperparameter optimization: Comparing genetic algorithm against grid search and bayesian optimization, *2021 IEEE congress on evolutionary computation (CEC)*, IEEE, 2021, pp. 1551–1559.

60 S. Rai, B. Pandey and D. Dwivedi, Device simulation of low cost HTM free perovskite solar cell based on TiO_2 electron transport layer, *AIP Conference Proceedings*, AIP Publishing, 2020.

61 M. K. Hossain, G. I. Toki, A. Kuddus, M. H. Rubel, M. Hossain, H. Bencherif, M. F. Rahman, M. R. Islam and M. Mushtaq, An extensive study on multiple ETL and HTL layers to design and simulation of high-performance lead-free $CsSnCl_3$-based perovskite solar cells, *Sci. Rep.*, 2023, **13**, 2521.

62 R. Jeyakumar, A. Bag, R. Nekovei and R. Radhakrishnan, Influence of electron transport layer (TiO_2) thickness and its doping density on the performance of $CH_3NH_3PbI_3$-based planar perovskite solar cells, *J. Electron. Mater.*, 2020, **49**, 3533–3539.

63 G.-W. Kim, D. V. Shinde and T. Park, Thickness of the hole transport layer in perovskite solar cells: performance versus reproducibility, *RSC Adv.*, 2015, **5**, 99356–99360.

64 A. Ahmed, K. Riaz, H. Mehmood, T. Tauqeer and Z. Ahmad, Performance optimization of $CH_3NH_3Pb(I_{1-x}Br_x)_3$ based perovskite solar cells by comparing different ETL materials through conduction band offset engineering, *Opt. Mater.*, 2020, **105**, 109897.

65 Y. An, A. Shang, G. Cao, S. Wu, D. Ma and X. Li, Perovskite solar cells: optoelectronic simulation and optimization (Sol. RRL 11/2018), *Sol. RRL*, 2018, **2**, 1870227.

66 F. Liu, J. Zhu, J. Wei, Y. Li, M. Lv, S. Yang, B. Zhang, J. Yao and S. Dai, Numerical simulation: toward the design of high-efficiency planar perovskite solar cells, *Appl. Phys. Lett.*, 2014, **104**, 253508.

67 S. Mahjabin, M. M. Haque, K. Sobayel, M. Jamal, M. A. Islam, V. Selvanathan, A. K. Assaifan, H. F. Alharbi, K. Sopian and N. Amin, Perceiving of defect tolerance in perovskite absorber layer for efficient perovskite solar cell, *IEEE Access*, 2020, **8**, 106346–106353.

68 M. M. Haque, S. Mahjabin, S. Khan, M. I. Hossain, G. Muhammad, M. Shahiduzzaman, K. Sopian and M. Akhtaruzzaman, Study on the interface defects of eco-friendly perovskite solar cells, *Sol. Energy*, 2022, **247**, 96–108.

69 M. Moustafa, Z. Abu Waar and S. Yasin, Optimizing solar performance of CFTSe-based solar cells using $MoSe_2$ as an innovative buffer layers, *Sci. Rep.*, 2025, **15**, 614.

70 T. Zhao, J. S. Beckwith, M. J. Amin, M. Pálmai, P. T. Snee, M. Tien and H. Yang, Leveraging lifetime information to perform real-time 3D single-particle tracking in noisy environments, *J. Chem. Phys.*, 2021, **155**, 164201.

71 M. K. Hossain, M. K. Mohammed, R. Pandey, A. Arnab, M. Rubel, K. Hossain, M. H. Ali, M. F. Rahman, H. Bencherif and J. Madan, Numerical analysis in DFT and SCAPS-1D on the influence of different charge transport layers of $CsPbBr_3$ perovskite solar cells, *Energy Fuels*, 2023, **37**, 6078–6098.

72 M. K. Hossain, D. Samajdar, R. C. Das, A. Arnab, M. F. Rahman, M. Rubel, M. R. Islam, H. Bencherif, R. Pandey and J. Madan, Design and simulation of Cs_2BiAgI_6 double perovskite solar cells with different electron transport layers for efficiency enhancement, *Energy Fuels*, 2023, **37**, 3957–3979.

73 X. Wang, W. Wang, J. Liu, J. Qi, Y. He, Y. Wang, W. Hu, Y. Cheng, K. Chen and Y. Hu, Reducing optical reflection loss for perovskite solar cells via printable mesoporous SiO_2 antireflection coatings, *Adv. Funct. Mater.*, 2022, **32**, 2203872.

74 R. Bernal-Correa and A. Morales-Acevedo, Spectral reflectance optimization for planar perovskite solar cells, *Optik*, 2021, **227**, 165973.

75 J. Qin, X.-K. Liu, C. Yin and F. Gao, Carrier dynamics and evaluation of lasing actions in halide perovskites, *Trends Chem.*, 2021, **3**, 34–46.

76 C. M. Wolff, S. A. Bourelle, L. Q. Phuong, J. Kurpiers, S. Feldmann, P. Caprioglio, J. A. Marquez, J. Wolansky, T. Unold and M. Stolterfoht, Orders of recombination in complete perovskite solar cells–linking time-resolved and steady-state measurements, *Adv. Energy Mater.*, 2021, **11**, 2101823.

77 J. Chantana, Y. Kawano, T. Nishimura, A. Mavlonov, Q. Shen, K. Yoshino, S. Iikubo, S. Hayase and T. Minemoto, Impact of Auger recombination on performance limitation of perovskite solar cell, *Sol. Energy*, 2021, **217**, 342–353.

78 Y. Nohara, K. Matsumoto, H. Soejima and N. Nakashima, Explanation of machine learning models using shapley additive explanation and application for real data in hospital, *Comput. Methods Programs Biomed.*, 2022, **214**, 106584.

79 M. T. Ekwu, E. Danladi, N. N. Tasie, I. S. Haruna, O. E. Okoro, P. M. Gyuk, O. M. Jimoh and R. C. Obasi, A Qualitative Theoretical Study of Inorganic HTM-Free $RbGeI_3$ Based Perovskite Solar Cells Using SCAPS 1D as a Pathway Towards 3.601% Efficiency, *East Eur. J. Phys.*, 2023, 118–124.

80 G. Pindolia, S. M. Shinde and P. K. Jha, Void of lead and non-carcinogenic germanium based $RbGeI_3$ PSC using organic charge transport layers: towards a clean and green future, *J. Mater. Sci.: Mater. Electron.*, 2023, **34**, 804.

81 M. A. Green, E. D. Dunlop, M. Yoshita, N. Kopidakis, K. Bothe, G. Siefer, D. Hinken, M. Rauer, J. Hohl-Ebinger and X. Hao, Solar cell efficiency tables (Version 64), *Prog. Photovolt.: Res. Appl.*, 2024, **32**, 425–441.

82 J. Li, H. Liang, C. Xiao, X. Jia, R. Guo, J. Chen, X. Guo, R. Luo, X. Wang and M. Li, Enhancing the efficiency and longevity of inverted perovskite solar cells with antimony-doped tin oxides, *Nat. Energy*, 2024, **9**, 308–315.